Article

Neuron

A Novel Mechanism for the Grid-to-Place Cell Transformation Revealed by Transgenic Depolarization of Medial Entorhinal Cortex Layer II

Highlights

- Depolarization of MECII neurons produces remapping in CA1 and impairs spatial memory
- Hyperpolarization of a similar number of MECII neurons produces neither
- Both manipulations change the firing rate, but not firing location, of MEC neurons
- Depolarization of MECII differentially changes firing rates of individual grid fields

Authors

Benjamin R. Kanter, Christine M. Lykken, Daniel Avesar, ..., Nils Z. Borgesius, Yasser Roudi, Clifford G. Kentros

Correspondence

clifford.kentros@ntnu.no

In Brief

Kanter et al. show that depolarization, but not hyperpolarization, of MECII neurons produces hippocampal remapping and impairs memory. Since MEC neurons do not change firing location, these results are likely due to changes in firing rate of individual grid fields.

Kanter et al., 2017, Neuron *93*, 1480–1492
March 22, 2017 © 2017 Elsevier Inc.
http://dx.doi.org/10.1016/j.neuron.2017.03.001

CellPress

CellPress

Neuron
Article

A Novel Mechanism for the Grid-to-Place Cell Transformation Revealed by Transgenic Depolarization of Medial Entorhinal Cortex Layer II

Benjamin R. Kanter,[1,2] Christine M. Lykken,[1,2] Daniel Avesar,[2] Aldis Weible,[2] Jasmine Dickinson,[2] Benjamin Dunn,[1] Nils Z. Borgesius,[1] Yasser Roudi,[1] and Clifford G. Kentros[1,2,3,*]

[1]Kavli Institute for Systems Neuroscience and Centre for Neural Computation, Norwegian University of Science and Technology, Olav Kyrres gate 9, 7030 Trondheim, Norway

[2]Institute of Neuroscience, University of Oregon, 1254 University of Oregon, Eugene, OR 97403, USA

[3]Lead Contact

*Correspondence: clifford.kentros@ntnu.no

http://dx.doi.org/10.1016/j.neuron.2017.03.001

SUMMARY

The spatial receptive fields of neurons in medial entorhinal cortex layer II (MECII) and in the hippocampus suggest general and environment-specific maps of space, respectively. However, the relationship between these receptive fields remains unclear. We reversibly manipulated the activity of MECII neurons via chemogenetic receptors and compared the changes in downstream hippocampal place cells to those of neurons in MEC. Depolarization of MECII impaired spatial memory and elicited drastic changes in CA1 place cells in a familiar environment, similar to those seen during remapping between distinct environments, while hyperpolarization did not. In contrast, both manipulations altered the firing rate of MEC neurons without changing their firing locations. Interestingly, only depolarization caused significant changes in the relative firing rates of individual grid fields, reconfiguring the spatial input from MEC. This suggests a novel mechanism of hippocampal remapping whereby rate changes in MEC neurons lead to locational changes of hippocampal place fields.

INTRODUCTION

Neurons in the hippocampal formation exhibit spatially selective activity patterns that are thought to support episodic memory and spatial navigation. Hippocampal place cells (O'Keefe and Dostrovsky, 1971) typically display single environment-specific spatial receptive fields that change drastically between different environments, a process referred to as remapping (Muller and Kubie, 1987). In contrast, grid cells in medial entorhinal cortex (MEC), one of two major inputs to the hippocampus, have multiple regularly spaced firing fields (Fyhn et al., 2004; Hafting et al., 2005) that are largely similar between environments (Fyhn et al., 2007). Other directionally modulated and speed-modulated cell types in MEC also retain their basic firing patterns between environments (Taube et al., 1990; Kropff et al., 2015). Thus, it appears that MEC neurons encode space in general, while hippocampal neurons encode particular locations in space.

Much of the excitement surrounding the discovery of grid cells came from their presumed ability to generate place cells. Under conditions that elicit remapping in place cells, grid cells shift and rotate their axes (Fyhn et al., 2007) and transiently increase in size and scale (Barry et al., 2012). Theoretical models have elucidated how such changes may lead to remapping in downstream hippocampal place cells (Rolls et al., 2006; Solstad et al., 2006; de Almeida et al., 2009; Savelli and Knierim, 2010). Demonstrating causality is more challenging because it is difficult to determine which changes in MEC are critical for place cell remapping, and which are epiphenomena evoked by changes in sensory inputs.

Several recent studies bring the assumption that grid cells are the primary determinant of place cell firing into question. Notably, pharmacological inactivation of the medial septum reduces theta power and disrupts the hexagonal regularity of grid cells, yet has surprisingly little effect on the stability of place fields in familiar environments (Koenig et al., 2011), or on their development in novel environments (Brandon et al., 2014). In addition, place fields are present several days before the emergence of grid firing patterns during development (Langston et al., 2010; Wills et al., 2010). Finally, a recent study reported that while grid cells form the majority of the direct projections from MEC to the hippocampus, other functionally specialized cell types such as border and head direction cells project directly to the hippocampus as well (Zhang et al., 2013). These findings lead to the counterintuitive suggestion that the spatial receptive fields of place cells do not rely on their major spatial input.

Indeed, it is still unclear exactly how the MEC network is involved in hippocampal spatial firing and spatial memory. Nearly complete entorhinal lesions do not prevent location-selective activity in the hippocampus, though the resulting place fields lack precision and spatial stability (Miller and Best, 1980; Brun et al., 2008; Van Cauter et al., 2008; Hales et al., 2014; Schlesiger et al., 2015). In addition, genetic disruptions and lesions of the entorhinal cortex produce impairments on some hippocampus-dependent tasks, but they can be milder than those

CrossMark

observed following lesions of the hippocampus (Parron et al., 2004; Steffenach et al., 2005; Yasuda and Mayford, 2006; Hales et al., 2014). A possible reason for these inconsistent results is that it is extremely difficult to surgically destroy the entirety of a structure without also damaging surrounding brain areas. Even ideal surgical lesions are irreversible and temporally diffuse, as the brain gradually adapts to the insult. More recent work has shown that hippocampal place fields change their firing properties to varying degrees following pharmacological (Ormond and McNaughton, 2015), chemogenetic (Miao et al., 2015; Zhao et al., 2016), and optogenetic (Miao et al., 2015; Rueckemann et al., 2016) inactivation of MEC. While these results provide support for the idea that MEC is involved in hippocampal spatial firing, the changes in the firing patterns of MEC neurons in response to these manipulations are not well characterized. Therefore, it is difficult to determine precisely which changes in the firing patterns of MEC neurons lead to changes in hippocampal place fields and spatial memory deficits. Finally, most of these interventions depend upon the complex diffusion of a bolus within the brain, which generates variability in the number and types of neurons affected in each animal (Lykken and Kentros, 2014).

To overcome these issues, we designed experiments using transgenic mice expressing DREADDs (Designer Receptors Exclusively Activated by Designer Drugs) (Alexander et al., 2009) almost exclusively in stellate cells of MEC layer II (MECII), where grid cells are most abundant (Sargolini et al., 2006). By using transgenic crosses rather than stereotactic injections into brain tissue, expression of the transgene was similar in all mice and we were able to estimate the percentage of each cell type being manipulated. Here, we present the electrophysiological and behavioral results of reversibly increasing or decreasing the membrane potential of a subset of MECII neurons, yielding insight into the relationship between the spatial firing properties of MEC and hippocampal neurons, and their relationship to spatial memory.

RESULTS

Anatomical Specificity of the Transgenic Crosses

One of the most attractive features of transgenic crosses is that they are anatomically restricted in a more uniform manner than injections of pharmacological or viral agents. Here, we crossed the EC-tTA driver line (Yasuda and Mayford, 2006) to hM3Dq- or hM4Di-tetO DREADD lines (Alexander et al., 2009) to enable control of neurons in the superficial layers of MEC via intraperitoneal injection of the designer ligand clozapine N-oxide (CNO). Double-positive offspring are referred to as hM3 and hM4 mice, respectively. The driver line expresses primarily throughout the dorsoventral extent of MECII, as well as in other brain regions such as pre- and parasubiculum, depending on the particular cross (Rowland et al., 2013; Yetman et al., 2016). DREADD receptor expression restricted to superficial MEC was revealed by antibody labeling of a heme-agglutinin (HA) epitope tag (Figure 1A), but localization of the receptor to processes made quantification nearly impossible. Therefore, to visualize somatic transgene expression, we performed in situ hybridization using a custom probe targeting DREADD receptor mRNA (hM3Dq: Figure 1B, hM4Di: Figure 1D). We quantified expression levels by counting the number of hM3Dq RNA-positive nuclei (Figure S1) within all brain regions with detectable expression levels (Figure 1C). We estimated that 20% of nuclei in MECII expressed the DREADD receptor in each transgenic cross. Our prior work (Rowland et al., 2013) demonstrated that this driver line expresses in stellate cells of MECII, which form the majority (74%) of nuclei in layer II (Gatome et al., 2010). Therefore, our manipulation targeted approximately 27% of layer II stellate cells, and relatively few other cell types. Since the only other areas with significant expression levels (pre- and parasubiculum) have very weak projections to the hippocampus (Köhler, 1985), we ascribe the vast majority of our effects on hippocampal neurons to the manipulation of MECII activity.

Depolarization, but Not Hyperpolarization, of MECII Causes "Artificial Remapping" in CA1

Naive adult mice were implanted with chronic tetrode arrays targeting hippocampal area CA1 (Figures S2A, S2C, S2E, and S2G) to record the effect of manipulating MECII activity on place cells. Depolarizing MECII inputs by CNO injection (1 mg/kg) in hM3 mice had striking effects on CA1 place cells in a stable, familiar environment (Figure 2). A large proportion of cells shifted the location of their place fields (28/105, or 27%, Figures 2A–2C), or had fields that turned on (9/105, or 9%, Figure 2D) or off (5/105, or 5%, Figure 2E), closely resembling the remapping observed between distinct environments. Other simultaneously recorded cells changed their firing rate and/or field size, but maintained the position of their primary field (19/105, or 18%, Figure 2F), much like the rate remapping seen between similar environments (Leutgeb et al., 2005). We refer to the above changes collectively as "artificial remapping." The remaining cells did not change significantly in any of these dimensions (Figure 2G), suggesting that some degree of the initial hippocampal representation was still intact.

At the population level, depolarization of MECII significantly increased firing rate (Figure 3A) and field size (Figure 3B) of CA1 place cells compared to littermate controls (rate: hM3 n = 80, Con n = 91, p = 0.02; size: hM3 n = 76, Con n = 91, $p = 8.04 \times 10^{-5}$; two-sided independent t tests). As a result of the increased field size, there was a concomitant decrease in spatial information relative to controls (Table S1), but the Gaussian structure of the fields remained intact (coherence: hM3 n = 80, Con n = 91, p = 0.72, one-sided Wilcoxon rank sum test). These firing rate and field size effects alone could indicate that MECII neurons simply provide gain control to the hippocampus. However, the spatial correlation of firing rate maps before and after CNO injection was significantly lower in hM3 mice relative to controls (hM3 n = 80, Con n = 91, $p = 4.31 \times 10^{-7}$, one-sided Wilcoxon rank sum test, Figure 3C), suggesting that substantial hippocampal remapping occurred even though the mouse remained in a stable, familiar environment. An alternative method of quantifying the extent of remapping revealed that while 83% (77/93) of place cells had spatial correlation values between the first and second halves of the baseline session that exceeded the 95th percentile of a shuffled distribution, only 26% (21/80) of place cells had correlation values between baseline and CNO sessions that passed the

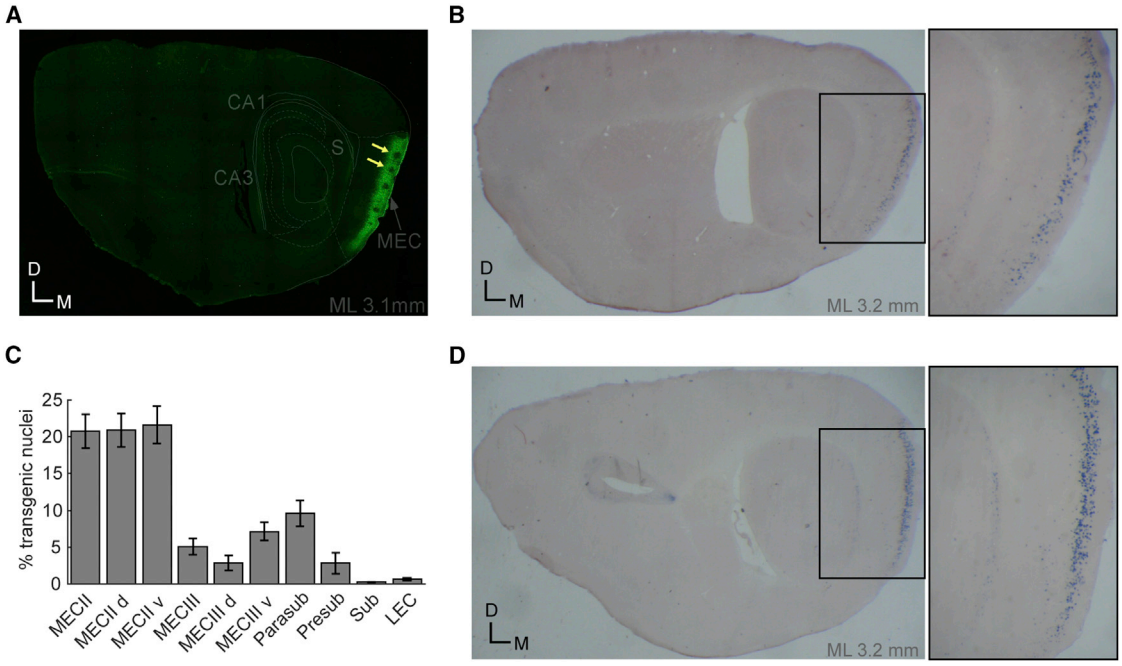

Figure 1. Transgenic Expression of DREADD Receptors Is Highly Specific to MECII

(A) Expression of hM3Dq transgene visualized by heme-agglutinin antibody in sagittal section. Note the absence of label in presumed calbindin-positive patches (yellow arrows), consistent with expression restricted to reelin-positive stellate cells. D, dorsal; M, medial; S, subiculum; ML, medial/lateral relative to midline.

(B) RNA in situ hybridization targeted to hM3Dq. Inset on right shows MEC.

(C) Percentage of hM3Dq-positive nuclei by brain region (mean ± SEM; n = 9 mice). MEC, medial entorhinal cortex; d, dorsal; v, ventral; Parasub, parasubiculum; Presub, presubiculum; Sub, subiculum; LEC, lateral entorhinal cortex. Roman numerals refer to cell layer.

(D) RNA in situ hybridization targeted to hM4Di. Inset on right shows MEC.

Magnification is 1.25×, and 4× for insets.

same threshold. To determine the time course of remapping, we divided the data into smaller temporal bins and found that the decrease in spatial correlation occurred 10–15 min post-injection (hM3 n = 81, Con n = 84, $p = 7.66 \times 10^{-5}$, one-sided Wilcoxon rank sum test, Figure S3A). Interestingly, this CNO-induced remapping stabilized over the duration of the 2-hr recording session (Figure S4). In addition, the effects were generally reversible, as the firing rate, field size, and spatial correlations were not significantly different from controls 12+ hr post-CNO injection (rate: hM3 n = 77, Con n = 91, p = 0.07, two-sided independent t test, Figure 3A; size: hM3 n = 72, Con n = 91, p = 0.83, two-sided independent t test, Figure 3B; spatial correlation: hM3 n = 77, Con n = 37, p = 1.00, one-sided Wilcoxon rank sum test, Figure 3C). While this may indicate that the altered place cell map is not consolidated, it is possible that it would be reinstated following a subsequent injection of CNO.

Given that depolarizing MECII produced these qualitative changes in place cell activity, we predicted that hyperpolarization of the same MECII inputs would yield similar results. However, we found that hyperpolarizing MECII had a negligible effect on CA1 place cells (e.g., Figure 2H), despite using a much higher dose of CNO (10 mg/kg) in an attempt to elicit an effect. Changes in mean firing rate, field size, and spatial information in hM4 mice were not significantly different from controls (rate: hM4 n = 106, Con n = 91, p = 0.28, Figure 3A; size: hM4 n = 102, Con n = 91, p = 0.46, Figure 3B; spatial information: hM4 n = 106, Con n = 91, p = 0.44, Table S1; two-sided independent t tests). In addition, there was no change in the spatial correlation between firing rate maps before and after injection of CNO relative to littermate controls (hM4 n = 106, Con n = 91, p = 0.93, one-sided Wilcoxon rank sum test, Figure 3C), indicating that this manipulation did not cause hippocampal remapping. Furthermore, the majority (78/106, or 74%) of place cells had spatial correlation values between baseline and CNO sessions that exceeded the 95th percentile of the shuffled distribution (BL first versus second half: 119/127, or 94%). Thus, it seems that place cells are not affected by transgenic hyperpolarization of MECII stellate cells, even though depolarization of a similar number of them results in drastic changes.

Behavioral Significance of Artificial Remapping

Since artificial remapping appears to reflect a major reorganization of the place cell code, we wanted to examine its impact on spatial memory. We trained naive cohorts of hM3, hM4, and littermate control mice (hM3 n = 13, hM4 n = 13, Con n = 25) in the Morris water maze. As expected, learning rates for both cued (non-spatial, Days 1–2) and hidden (spatial, Days 6–8) versions of the task did not differ between groups (cued: p = 0.71; hidden: p = 0.17; one-between one-within ANOVA; Figure 4A). However, CNO injection 30 min before the probe test on Day 9 significantly increased the escape latency in hM3, but not hM4,

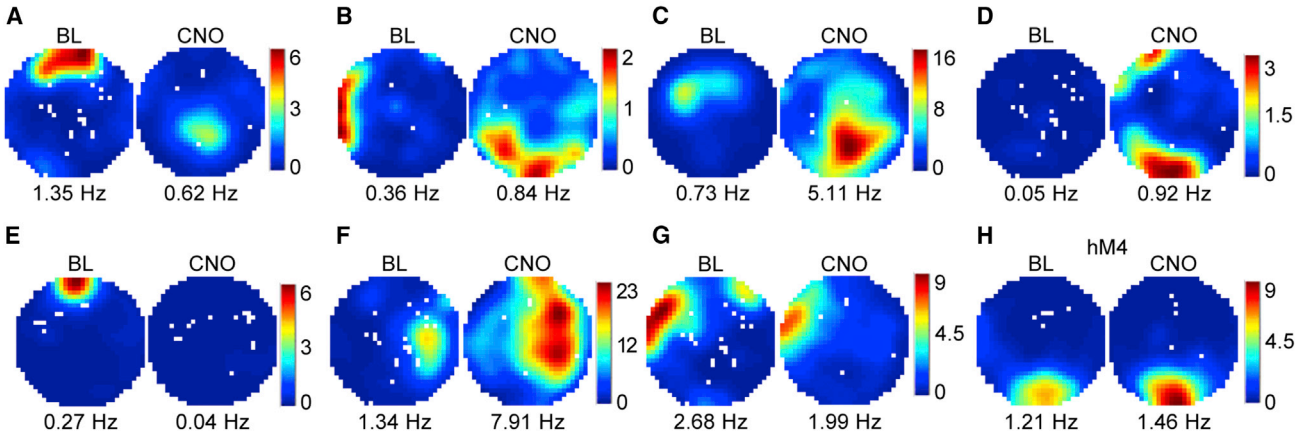

Figure 2. Artificial Remapping of CA1 Place Cells following Depolarization, but Not Hyperpolarization, of MECII

(A–G) Firing rate maps of seven representative CA1 place cells in hM3 mice before and after CNO injection. Rate maps show that place cells changed location and shape (A–C), turned on (D), turned off (E), expanded (F), or were unaffected (G) following CNO injection. Cells in (A), (D), (F), and (G) were simultaneously recorded. (H) Rate maps of a representative place cell from an hM4 mouse that was unaffected by CNO injection.

BL, baseline; CNO, 30–60 min post-CNO injection. Maps are scaled to maximum rate between sessions. Red represents maximum firing, blue is silent, and white represents unvisited pixels. Mean rate indicated below rate maps.

mice relative to controls (hM3: $p = 0.02$; hM4: $p = 0.31$; one-sided Wilcoxon rank sum tests; Figure 4B). This increased latency cannot be explained by reduced swimming speed in hM3 mice (hM3 versus Con: $p = 0.30$, one-sided Wilcoxon rank sum test). Moreover, hM3 mice spent significantly less time in the target quadrant compared to control mice ($p = 0.01$, one-sided Wilcoxon rank sum test). When injected with vehicle on Day 10, hM3 mice found the target as quickly as hM4 and control mice (hM3 versus hM4: $p = 0.47$; hM3 versus Con: $p = 0.83$; one-sided Wilcoxon rank sum tests; Figure 4C), indicating that they were able to successfully retrieve the memory of the platform location. This result is consistent with the return to baseline firing patterns observed after CNO has worn off. Thus, artificial remapping of place cells via depolarization, but *not* hyperpolarization, of a subset of hippocampal inputs is sufficient to impair recall of a previously formed spatial memory.

Manipulation of MECII Activity Leads Only to Quantitative Changes in MEC Neurons

The surprising dichotomy between these manipulations made it imperative to uncover exactly how upstream MEC neurons respond to CNO administration. Naive cohorts of hM3 and hM4 mice were implanted with chronic tetrode arrays targeting the superficial layers of dorsal MEC (Figures S2B, S2D, S2F, and S2H). Recordings of MEC neurons before and after CNO administration were performed under conditions nearly identical to those of the hippocampal recordings. Depolarization of MECII neurons in hM3 mice significantly increased firing rate (e.g., Figures 5A, 5C, and 5D) and field size (e.g., Figure 5A) of putative excitatory MEC neurons relative to controls (e.g., Figure 5E) (rate: hM3 $n = 86$, Con $n = 28$, $p = 4.79 \times 10^{-3}$, Figure 6A; size: hM3 $n = 74$, Con $n = 40$, $p = 2.14 \times 10^{-7}$, Figure 6B; one-sided Wilcoxon rank sum tests). The time course of this rate increase closely mirrored that of the CNO-induced remapping in CA1, occurring 10–15 min post-injection (hM3 $n = 95$, Con $n = 25$, $p = 0.01$, one-sided Wilcoxon rank sum test, Figure S3B). Surprisingly, CNO administration did not alter the location of the firing fields of excitatory MEC neurons (e.g., Figures 5A–5C) (hM3 $n = 82$, Con $n = 49$, $p = 0.29$, one-sided Wilcoxon rank sum test, Figure 6C). Counterintuitively, this result implies that the extensive hippocampal remapping observed in hM3 mice is caused by nonspatial changes in MEC inputs.

Since CNO injection in hM4 mice did not lead to hippocampal remapping, we assumed that its direct effects on MEC neurons would also be minimal. However, transgenic hyperpolarization of MECII in hM4 mice significantly decreased firing rate (e.g., Figure 5F) and field size of putative excitatory MEC neurons compared to controls (rate: hM4 $n = 71$, Con $n = 28$, $p = 2.15 \times 10^{-5}$, Figure 6A; size: hM4 $n = 61$, Con $n = 40$, $p = 0.01$, Figure 6B; one-sided Wilcoxon rank sum tests). Similarly, there was no significant difference in the spatial correlation of firing rate maps before and after CNO injection between hM4 and control mice (hM4 $n = 69$, Con $n = 49$, $p = 0.16$, one-sided Wilcoxon rank sum test, Figure 6C). Therefore, our manipulations of MECII neurons bidirectionally affected firing rate and field size of excitatory MEC neurons without any obvious changes to their spatial firing patterns. This raises the question of how depolarization and hyperpolarization of a similar number of MECII neurons have comparable effects on the firing of MEC neurons, yet drastically different effects on the hippocampus.

The simplest explanation would be that depolarization of MECII stellate cells leads to larger quantitative changes in putative excitatory MEC neurons than their hyperpolarization, but the magnitude of firing rate and field size changes were nearly identical between hM3 and hM4 mice (Figures 6A and 6B). A more detailed analysis revealed a subtle difference between the crosses. As expected, hyperpolarization of MECII neurons led to an overall decrease in firing rate of excitatory MEC neurons, with cells either firing less or not changing (Figure 6D), presumably reflecting cells that did or did not express the transgene,

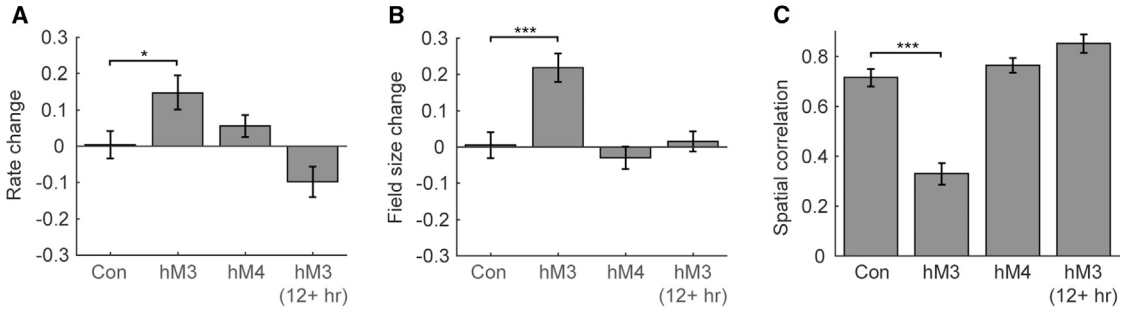

Figure 3. Depolarization, but Not Hyperpolarization, of MECII Reversibly Increases Firing Rate and Field Size of CA1 Place Cells and Induces Artificial Remapping

(A and B) Change in mean firing rate (A) and field size (B) following CNO injection in littermate control (Con), hM3, and hM4 mice.

(C) Spatial correlation between baseline and CNO sessions in Con, hM3, and hM4 mice.

Rightmost bars compare the baseline and 12+ hr post-CNO injection sessions in hM3 mice and show return to baseline firing patterns. Data represented as median ± SEM. *$p < 0.05$, ***$p < 0.001$. Change refers to a difference score (see STAR Methods).

respectively. Surprisingly, depolarization elicited bidirectional changes in firing rate (Figure 6D). The majority of excitatory cells increased their firing rate, but a substantial number of cells decreased their rate after CNO injection, resulting in significantly larger variance in rate changes in hM3 versus hM4 mice (hM3 n = 86, hM4 n = 71, $p = 3.35 \times 10^{-3}$, Levene's test). A recent imaging study (Kitamura et al., 2015) also reported that MEC cells drastically increased or decreased their firing rates between distinct environments. Approximately 36% of MECII stellate cells were significantly more active in one environment and were dubbed "context cells." When we calculated an analogous firing rate threshold, we found that merely 7% (6/90) of cells in hM3 mice and only 1% (1/84) of cells in hM4 mice were significantly more active either before or after CNO injection (includes putative excitatory and inhibitory cells, Figure S5). While Kitamura et al. (2015) did not address the functional characteristics of the neurons they imaged, the cells we identified were not of a particular functional class of MEC neurons. Furthermore, the observed firing rate changes appear to be the tails of a continuous distribution, rather than representing a separate population of MEC cells.

If artificial remapping is driven by changes in a specific functional cell type or set of cell types in MEC, the above analyses may have occluded differences between hM3 and control mice by grouping all putative excitatory neurons together. Since we do not know which functional cell types express our transgenic receptors, we examined the previously characterized functional classes individually. Surprisingly, we did not observe any large changes in the location of grid cell firing fields by translation or rotation (Figures 7A–7C; Table S2), which are the most obvious effects observed under conditions that elicit hippocampal remapping (Fyhn et al., 2007). Furthermore, grid regularity and scale, which have previously been shown to change upon introduction to a novel environment (Barry et al., 2012), remained essentially unchanged following transgenic depolarization (Table S2). Interestingly, we discovered that the average change in firing rate of grid cells following CNO injection in hM3 mice was not significantly different from controls (Table S2) because grid cells were among the MEC neurons described above that exhibited bidirectional rate changes (increase: 9/21; decrease 8/21; compared to 95th percentile of control distribution; e.g., Figures 5A and 5B). This was not the case for grid field size, which increased or remained stable (max field size: increase = 11/18, stable = 7/18; compared to 95th percentile of control distribution). Border (or boundary-vector) cells (e.g., Figure 5C) increased in firing rate (n = 14, Table S2) and field size (n = 13, median difference score = 0.34) following transgenic depolarization, but did not shift their preferred environmental boundary (n = 14, median spatial correlation = 0.67). Finally, head direction cells (e.g., Figure 5D) significantly increased their firing rate without changing their directional preference (n = 58, Table S2), which is in direct contrast to changes observed during hippocampal remapping (Taube et al., 1990). Taken together, these results suggest that the changes in place field location observed in CA1 were likely not a result of changes in the spatial or directional properties of a specific functional cell type in MEC. Instead, it appears that depolarizing MECII neurons caused the majority of excitatory MEC neurons to change their firing rate and/or field size (i.e., quantitative, not qualitative changes), unlike the drastic spatial reorganization observed downstream in the hippocampus (Figures 2 and 3).

Potential Mechanisms of Artificial Remapping

Given that grid cells are the most abundant spatial input to the hippocampus, and that they exhibited bidirectional firing rate changes following depolarization of MECII, we focused our subsequent analyses on grid cells. To determine whether the observed changes in grid cell firing rates alone were capable of eliciting remapping in hM3 mice, we simulated our results in a simple linear summation model of the grid-to-place cell transformation (Solstad et al., 2006). The simulation was run once where each grid cell had uniform peak firing rates, as previously published. The simulation was then repeated after scaling 20% (consistent with transgene expression levels) of the grid cells' firing rates to match the empirical data from hM3 and control mice following injection of CNO. These firing rate changes were not sufficient to cause place cell remapping (median spatial correlations: hM3 = 0.96, Con = 1.00), demonstrating the need

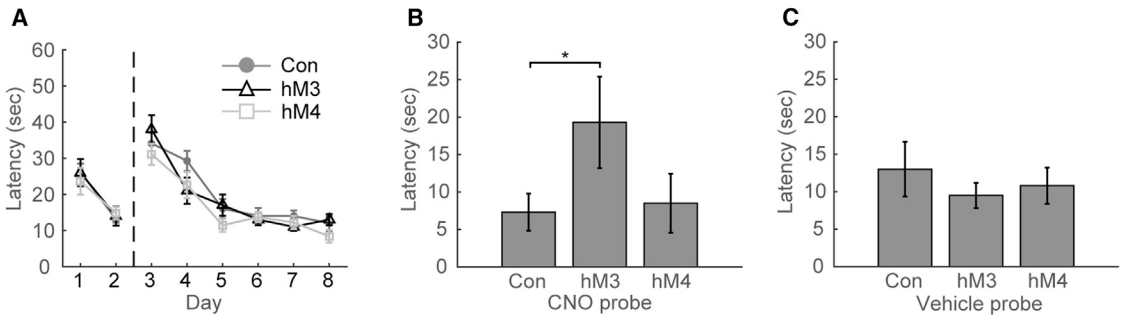

Figure 4. Spatial Memory Is Transiently Impaired following Depolarization, but Not Hyperpolarization, of MECII

(A) No difference in escape latency across training days between Con (dark gray circles), hM3 (black triangles), and hM4 mice (light gray squares). Vertical dashed line divides cued and hidden versions of task.

(B) Significant increase in escape latency following CNO injection during probe test on Day 9 in hM3, but not hM4 or Con mice.

(C) No difference in escape latency following vehicle injection during probe test on Day 10 between Con, hM3, and hM4 mice.

Data represented as median ± SEM. *$p < 0.05$.

for a shift in the location of grids relative to each other to cause remapping in this model.

Thus, the above analyses of MEC activity do not provide a clear explanation for the artificial remapping observed in hM3 mice. Since our sole manipulation was the depolarization of a minority of MECII stellate cells, there must be some aspect of MEC activity that produces sufficient change in spatial input to the hippocampus to elicit remapping. As previously described, we observed significant CNO-induced changes in firing rate without changes in firing location in MEC (i.e., rate remapping, Figures 6 and 7). While we initially examined these measures at the level of single neurons, the relevant information about space may be encoded at the population level. We therefore computed a population vector (PV) correlation of all recorded MEC neurons, which captures changes in both firing rate and location (Leutgeb et al., 2005). As expected, PV correlations for excitatory MEC neurons in hM3 mice were significantly lower than in controls, reflecting the CNO-induced firing rate changes reported above (Table S2). In order to determine whether grid cells in particular convey spatial change through firing rate alone, we computed PV correlations for grid cells and all other excitatory (non-grid) cells separately. Interestingly, while PV correlations for grid and non-grid cells were very similar in both control and hM4 mice, they were much lower for grid versus non-grid cells in hM3 mice (median PV correlation: Con grid = 0.94, Con non-grid = 0.88, hM4 grid = 0.76, hM4 non-grid = 0.79, hM3 grid = 0.35, hM3 non-grid = 0.63; Figures 7D and 7E). These results demonstrate that grid cell firing rates are very stable between repeated exposures to the same environment, yet change drastically during hippocampal remapping. We thus provide the first empirical evidence that grid cells can encode spatial change without changing spatial location (i.e., translation or rotation of grid fields).

This seeming contradiction is resolved if the firing rates of individual grid fields change independently. We calculated the CNO-induced rate changes of individual grid fields, rather than looking at each grid pattern as a whole, as is typically done. In hM3 mice, CNO administration led to changes in individual grid field firing rates that differed in magnitude and/or direction within a single cell. Some hM3 grid cells had fields that responded bidirectionally to CNO, thus changing the relative rankings between fields (5/17 cells, Figure 8A). The remaining hM3 grid cells had fields that all changed rate in the same direction, but to varying degrees (12/17; 9/12 increase, 3/12 decrease; Figure 8A). In control mice, there was a negligible change in firing rate within the fields (Figure 8A), consistent with the idea that the rates of individual grid fields are stable across repeated exposures to a familiar environment. This disruption in the relationship between grid field firing rates in hM3 mice can be observed at the population level by comparing the grid field rate changes within the baseline session to those between the baseline and CNO sessions. The peak firing rates of individual fields were highly correlated between the first and second halves of the baseline session for hM3, hM4, and control mice (hM3: $n = 77$, $p = 1.86 \times 10^{-23}$; hM4: $n = 23$, $p = 3.96 \times 10^{-8}$; Con: $n = 37$, $p = 6.05 \times 10^{-13}$; linear correlations). However, the firing rates of individual grid fields before and after CNO injection were not correlated for hM3 mice ($n = 75$, $p = 0.11$, linear correlation, Figure 8B), yet remained strongly correlated for control ($n = 40$, $p = 2.25 \times 10^{-13}$, linear correlation, Figure 8B) and hM4 mice ($n = 28$, $p = 0.01$, linear correlation). We then examined the relationship between grid field firing rates on a cell-by-cell basis. For each grid cell, the variance of the CNO-induced rate changes of individual fields indicates the degree to which the fields change independently. In hM3 mice, grid cells had significantly greater field rate change variability compared to those of control mice (hM3 $n = 16$, Con $n = 8$, $p = 0.02$, one-sided Wilcoxon rank sum test, Figure 8C), which was not the case in hM4 mice (hM4 $n = 6$, Con $n = 8$, rank sum = 46, $p = 0.47$, one-sided Wilcoxon rank sum test).

This striking difference in individual grid field rates in hM3 mice is potentially very significant. If the firing rate relationships of grid fields are stable in a familiar environment, but change under conditions that elicit place cell remapping, then grid cells may provide a contextual signal that triggers remapping. One should therefore be able to decode context by sampling a sufficient number of grid cells. We tested this hypothesis by creating population vectors of all grid cells from hM3 and control mice for three recording epochs: baseline (BL), 30–60 min post-CNO

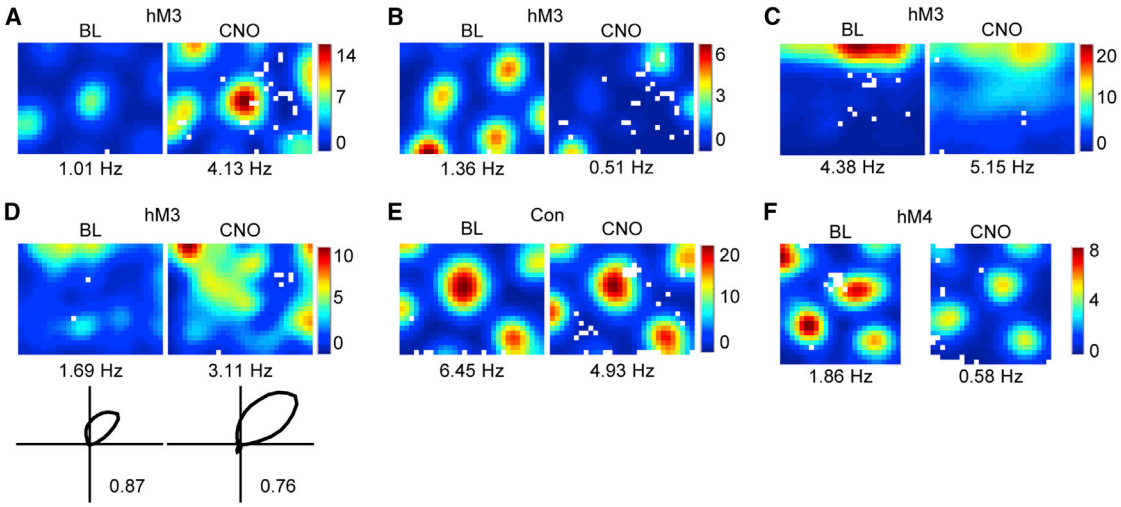

Figure 5. Altered Firing Rate of MEC Neurons following CNO Injection in hM3 and hM4 Mice

(A and B) Rate maps of grid cells in hM3 mice with increased (A) or decreased (B) firing rate and stable grid field locations following CNO injection.

(C) Border cell in an hM3 mouse with increased firing rate and preserved border representation following CNO injection.

(D) Head direction cell in an hM3 mouse with increased firing rate and preserved directional tuning following CNO injection. Mean vector length indicated below polar plots.

(E) Grid cell in a Con mouse that was unaffected by CNO injection.

(F) Grid cell in an hM4 mouse with decreased firing rate and stable grid field locations following CNO injection.

(A–F) Same convention used for Figure 2.

injection (CNO1), and 60–90 min post-CNO injection (CNO2). We reasoned that if grid field firing rates in hM3 mice change after CNO injection and then remain stable, the firing rates during CNO1 should be more similar to CNO2 than to BL. We sampled increasing numbers of grid cells and calculated the proportion of spatial bins for which this is true in hM3 and control mice. A decoding performance of 1 indicates that all CNO1 bins are more similar to CNO2, 0 indicates that all CNO1 bins are more similar to BL, and 0.5 indicates a failure to distinguish between BL and CNO2. Remarkably, we were able to successfully decode context in hM3 mice (Figure 8D), even with a small number of grid cells. However, we were not able to do so in control mice, indicating that simply removing the mouse from the environment to give it an injection is not sufficient to alter grid field firing rates. It is important to note that any changes in the relationship between the firing rates of individual grid fields is in fact a change in the spatial information conveyed by that cell, even without any change in the location of the fields. Thus, if this happens during "natural" remapping as well, grid cells could provide sufficiently distinct spatial input to the hippocampus to cause remapping without shifting relative to each other, consistent with all evidence to date (Fyhn et al., 2007; Barry et al., 2012).

DISCUSSION

We bidirectionally manipulated the excitability of a subset of hippocampal input neurons in MECII while examining the effects locally in MEC, downstream in CA1, and behaviorally in the water maze. We found that MEC neurons responded *quantitatively* to transgenic depolarization or hyperpolarization of MECII neurons by altering their firing rate and field size without changing the spatial location of their firing fields or their directional preferences. Two synapses downstream, however, hippocampal place cells in CA1 exhibited *qualitative* changes in their firing fields (i.e., remapping) in response to transgenic depolarization, but not hyperpolarization, of MECII neurons. The fact that depolarizing MECII neurons had drastically stronger downstream effects than hyperpolarizing the same cell types provides insight into the network mechanisms by which changes in MEC activity lead to remapping. Moreover, only depolarization of MECII caused spatial memory deficits in the water maze, highlighting the link between place cell activity and memory.

Our results are arguably the clearest demonstration to date of how manipulating the activity of MEC neurons produces hippocampal remapping and which changes in these two brain regions are associated with impairments in spatial memory. Lesions of the entorhinal cortex have previously been shown to result in imprecise and unstable place fields (Miller and Best, 1980; Brun et al., 2008; Van Cauter et al., 2008; Hales et al., 2014; Schlesiger et al., 2015), as well as spatial memory impairments on hippocampus-dependent tasks (Parron et al., 2004; Steffenach et al., 2005; Hales et al., 2014). While these studies indicate a clear role for the entorhinal cortex in hippocampal spatial firing and spatial memory, they are limited by their inability to determine precisely how the entorhinal cortex is involved in these functions in the intact brain. Additionally, several recent studies have demonstrated that inactivating MEC to varying degrees leads to hippocampal remapping (Miao et al., 2015; Ormond and McNaughton, 2015; Rueckemann et al., 2016). However, it is difficult to make strong conclusions about the mechanisms underlying remapping without fully understanding the effects of the manipulations in MEC. Moreover, these experiments rely upon

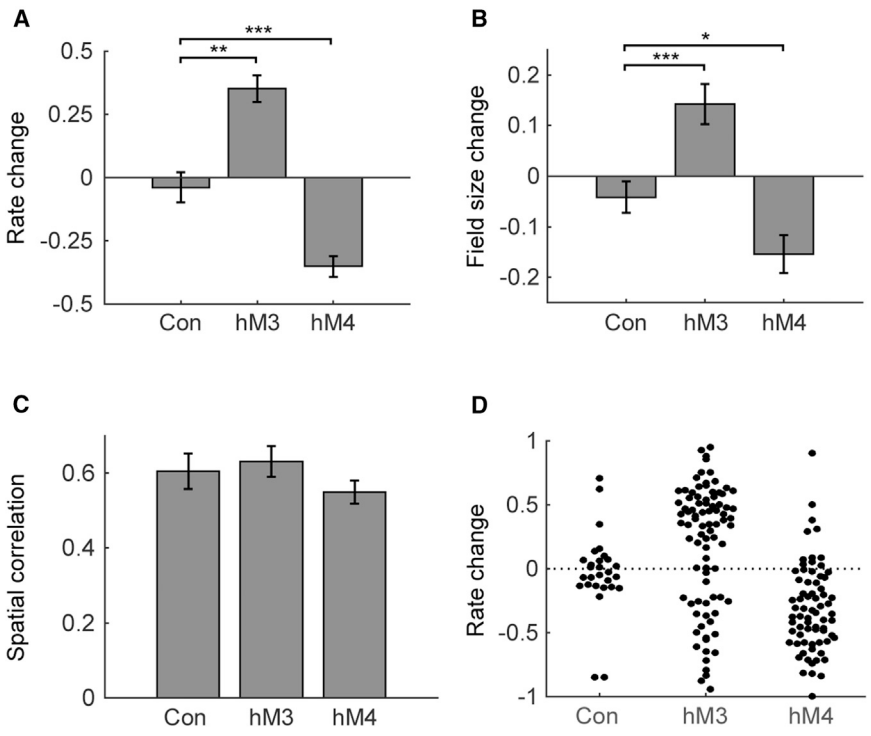

Figure 6. Depolarization and Hyperpolarization of MECII Neurons Produce Changes in Firing Rate and Field Size of Putative Excitatory MEC Neurons without Changing Spatial Location of Firing Fields

(A and B) Change in mean firing rate (A) and field size (B) following CNO injection in Con, hM3, and hM4 mice.

(C) Spatial correlation between baseline and CNO sessions in Con, hM3, and hM4 mice.

(A–C) Data represented as median ± SEM. *$p < 0.05$, **$p < 0.01$, ***$p < 0.001$.

(D) Change in mean firing rate for each cell following CNO injection in Con, hM3, and hM4 mice. Note bidirectional rate changes in hM3, but not hM4, mice. Dashed line indicates no rate change.

the diffusion of drugs or virus so the affected cell types cannot be precisely determined, nor do they address the relationship between remapping and spatial memory impairment. Only one study (Zhao et al., 2016) used a transgenic approach analogous to that presented here to hyperpolarize MEC neurons. This manipulation produced hippocampal remapping and disrupted spatial memory performance in the water maze. However, the expression pattern was not restricted to MEC, and most importantly, the authors did not characterize the in vivo responses of MEC neurons during their manipulation. It is unclear why these studies observed remapping after hyperpolarization of MEC, while we found that only depolarization causes remapping. The difference may be due to a combination of which cell types are affected and the strength of the inactivation of those neurons. A strength of our study is that we not only know the extent to which we manipulated a defined subset of stellate cells, but we also show which changes in the MEC network cause remapping and spatial memory impairment, and which changes do not. We clearly demonstrate that only the MECII manipulation that causes hippocampal remapping impairs spatial memory.

Other studies have infused drugs into the medial septum, thereby disrupting cholinergic signaling throughout the brain (Brandon et al., 2011, 2014; Koenig et al., 2011). This manipulation diminishes the spatial periodicity of grid cells and reduces the firing rate of all functional types of MEC neurons (except head direction cells). Nevertheless, place cells remain stable in familiar environments (Koenig et al., 2011), suggesting that intact grid firing patterns are not needed for the existence of place fields. Furthermore, their results demonstrate that decreasing the firing rate of MEC neurons does not necessarily elicit hippocampal remapping, as we observed in hM4 mice. In a subsequent study using a similar manipulation, they found that place cells can still remap in a novel environment (Brandon et al., 2014), indicating that the generation of new place fields also does not require spatially periodic grid cells. An important distinction between the aforementioned studies and our own work is that our manipulations do not degrade the grid pattern or change the location of grid fields. Thus, it may be that when the hippocampus is deprived of its dominant spatial input (through lesions or disruption of grid periodicity), it is capable of generating place fields on its own, as is the case during development. However, the hippocampus is likely sensitive to changes in MEC activity when its spatial inputs remain intact. Indeed, it is difficult to believe that spatial firing fields in the hippocampus do not depend upon their dominant spatial inputs.

Although artificial remapping is inherently distinct from natural remapping since the inputs to entorhinal cortex are unchanged, our results help elucidate which changes in MEC neurons are sufficient to cause remapping. Remarkably, transgenic depolarization of a subset of MECII neurons resulted in remapping without changing the firing locations of MEC neurons. This is in sharp contrast to the coherent shifts and rotations of grid patterns seen in distinct familiar environments (Fyhn et al., 2007). If one assumes a linear summation model of grid-to-place cell activity (Solstad et al., 2006), then this movement of firing fields could change which grid cells are coactive, thus leading to different place fields in the hippocampus. However, grid cells within a module (Stensola et al., 2012) shift and rotate coherently between distinct environments (Fyhn et al., 2007) such that their relationships are preserved. Since this presumably does not cause remapping, it has been proposed that distinct grid modules may shift relative to each other (Monaco and Abbott, 2011), but this remains to be observed experimentally. It has also been shown that grid fields temporarily expand in both size and scale and that the grid pattern becomes less regular upon introduction to a novel environment (Barry et al., 2012). While we did observe an increase in the size of spatial receptive fields in MEC, we found no significant changes in grid scale or

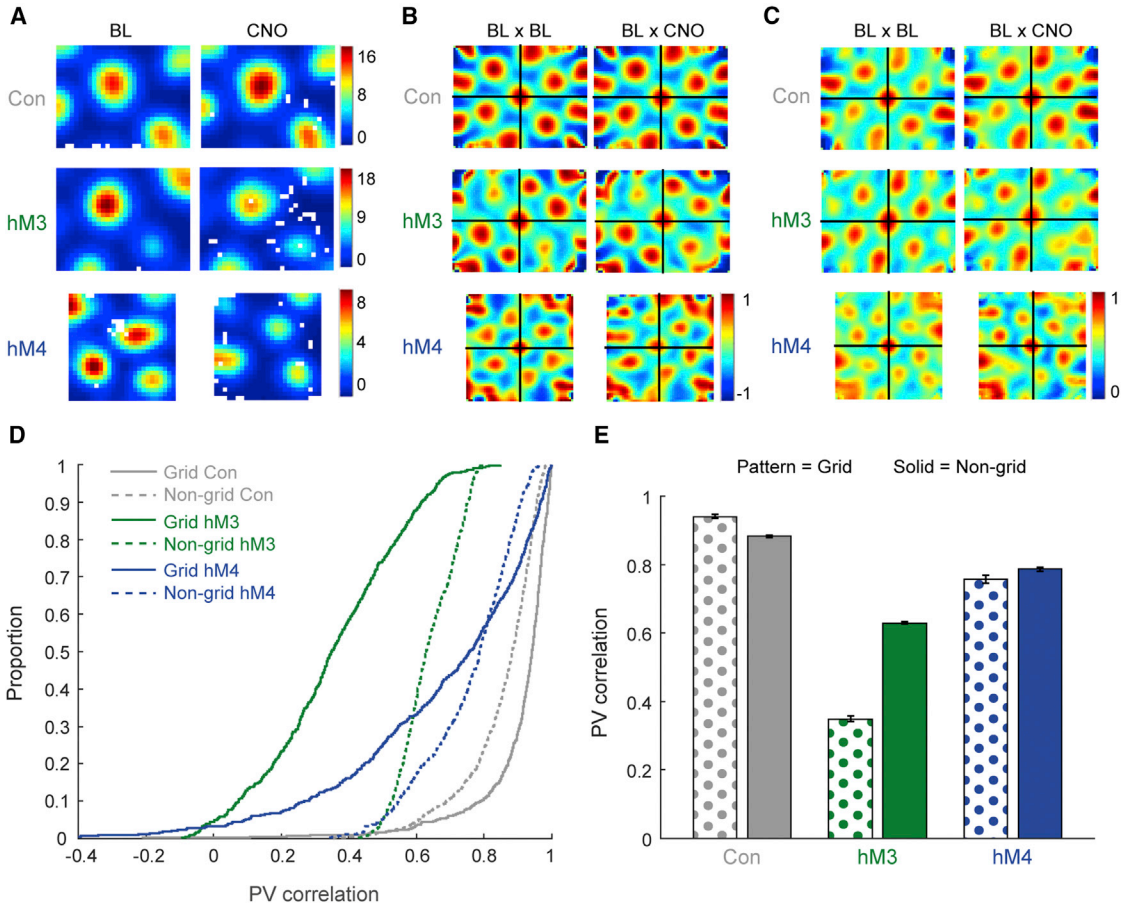

Figure 7. Rate Remapping in Grid Cells following Depolarization of MECII Conveys Spatial Change without a Shift in Grid Field Location

(A) Rate maps before and after CNO injection from Con (top), hM3 (middle), and hM4 (bottom) mice. Same convention used for Figure 2.

(B) Autocorrelograms (BL × BL) and cross-correlograms (BL × CNO) showing stable grid field locations after CNO injection for all example neurons in (A). Red represents maximum correlation and blue represents anti-correlation.

(C) Autocorrelograms (BL × BL) and cross-correlograms (BL × CNO) showing stable grid field locations after CNO injection for an ensemble of grid cells in Con (top, 3 cells), hM3 (middle, 7 cells), and hM4 (bottom, 6 cells) mice. (Note: hM4 grid cells were not simultaneously recorded.) Red represents maximum correlation and blue represents no correlation.

(D) Cumulative distribution functions for population vector (PV) correlations between baseline and CNO sessions in grid and non-grid cells in Con, hM3, and hM4 mice. Solid gray, grid Con; dashed gray, non-grid Con; solid green, grid hM3; dashed green, non-grid hM3; solid blue, grid hM4; dashed blue, non-grid hM4.

(E) Median PV correlations ± SEM between baseline and CNO sessions in grid and non-grid cells in Con, hM3, and hM4 mice. Note that grid cells strongly rate remap compared to non-grid cells in hM3, but not in Con or hM4 mice. Patterned bars, grid cells; solid bars, non-grid cells.

regularity, and it is unclear how an increase in field size alone could lead to remapping in the hippocampus. Transgenic depolarization of MECII also did not produce any significant changes in the firing patterns of border or head direction cells, which maintained their representation of environmental boundaries and directional tuning, respectively. Thus, it is unclear which, if any, of the previously observed changes in MEC are responsible for producing not only artificial remapping, but also natural remapping.

Our most puzzling finding is that both hyperpolarization and depolarization altered the average firing rates of MEC neurons to a similar degree, but only depolarization caused hippocampal remapping. An important difference between these manipulations is that only depolarization led to both increases and decreases in the firing rate of MEC neurons, resulting in greater variability in rate changes relative to the hyperpolarization-induced rate decreases. This paradoxical response to depolarization of MECII stellate cells strongly suggests a shift in the local interneuron network. Several studies have shown that layer II stellate cells are primarily connected via inhibitory interneurons (Dhillon and Jones, 2000; Couey et al., 2013; Pastoll et al., 2013) and that coordinated activity of multiple stellate cells engages this inhibitory network to inhibit other stellate cells (Couey et al., 2013), as we observed here. In contrast, since the basal activity of interneurons is likely not solely sustained by stellate cell activity, hyperpolarizing stellate cells may not be sufficient to disinhibit downstream excitatory neurons. Approximately half of the inhibitory neurons in MEC are parvalbumin-positive (PV+) interneurons (Wouterlood et al., 1995; Miettinen et al., 1996), which are perfectly suited to act as a network switch

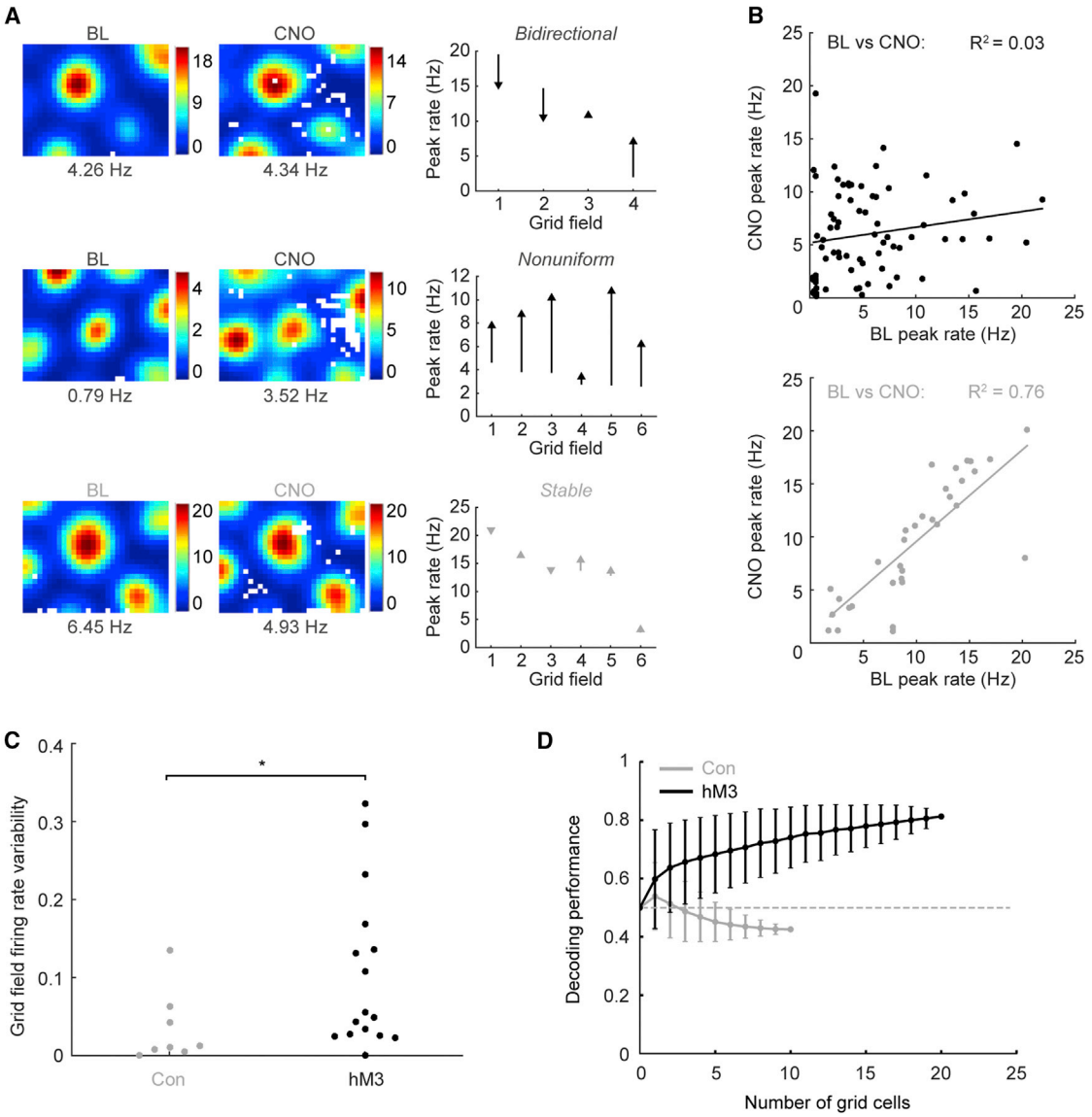

Figure 8. Altered Firing Rate Relationships between Individual Grid Fields Are Observed Only during Artificial Remapping, Potentially Providing a Contextual Signal to the Hippocampus

(A) Rate maps of three representative grid cells before (left) and after (middle) CNO injection. Each row is a cell. Same convention used for Figure 2. Rightmost column shows magnitude and direction of peak firing rate change for each grid field. Each arrow starts at BL rate and ends at CNO rate. Bidirectional (5/17 grid cells, right, top) and nonuniform changes (12/17 grid cells, right, middle) in individual grid field peak firing rates following CNO injection in an hM3 mouse. Stable firing rates (right, bottom) in individual grid fields following CNO injection in a Con mouse.

(B) Peak firing rates of individual grid fields change unpredictably following CNO injection in hM3 mice (top), but remain stable in Con mice (bottom).

(C) CNO-induced rate changes in individual grid fields are significantly more variable within a single grid cell in hM3 (black) versus Con (gray) mice. *$p < 0.05$.

(D) Decoding performance as a function of the number of sampled grid cells for hM3 (black) and Con (gray) mice. Gray dashed line indicates chance decoding performance. Data represented as mean ± standard deviation.

due to their connectivity and intrinsic electrical properties (Ferrante et al., 2016). Compared to other interneurons in MEC, PV+ cells are the most hyperpolarized at rest, but are capable of entering a sustained spiking regime. Furthermore, they inhibit all of the known functional cell types in MEC (Buetfering et al., 2014). Describing stellate cells as communicating via interneurons that act as rectifiers (i.e., they respond more readily to increases in input than to decreases) is therefore a useful simplification in an attempt to understand how MEC may create unique representations for distinct environments by triggering distinct network states. Moreover, computational modeling of cortical neurons as rectifiers has the advantage of easily creating sparse representations in a neural network (Glorot et al., 2011). The question nevertheless remains how this shift in the local network

state translates to changes in spatial firing downstream in the hippocampus.

There is still a large gap in the literature concerning how MEC neurons represent environmental context and how this information influences location selectivity in the hippocampus. One possibility is that the contextual signal in MEC may simply be encoded via population firing rate. In support of this idea, a recent imaging study reported the presence of "context cells" (reelin-positive stellate cells) in MECII, which exhibited significantly different firing rates in distinct environments (Kitamura et al., 2015). We observed cells with significant CNO-induced rate changes compared to controls, but we found a much lower proportion than previously reported (7% versus ~36% by Kitamura et al., 2015). Of course, this could be because we only targeted a subset of stellate cells and thus did not elicit remapping in all place cells. It is unknown whether these proposed context cells are of a particular functional class; however, a more recent electrophysiological study reported that all known functional types in MEC can alter their firing rate in response to changes in visual information (Pérez-Escobar et al., 2016). Indeed, it could be that other functional cell types such as boundary vector cells contribute to remapping (Barry et al., 2006). However, it is difficult to see how the changes that we observed in non-grid cells could result in hippocampal remapping.

Given their prominence in the network and their high spatial selectivity, grid cells are an attractive candidate to signal the need for a distinct place cell code. As mentioned above, it is possible that the contextual signal lies in the changes in the relationships between different grid cell modules (Monaco and Abbott, 2011). From a decoding perspective, grid cells provide highly accurate spatial information, while place cells provide contextual information (Wilson and McNaughton, 1993; Fiete et al., 2008; Sreenivasan and Fiete, 2011; Mathis et al., 2012; Stemmler et al., 2015). Therefore, place cell activity strongly indicates which environment the animal is in, while grid cell activity precisely indicates the animal's location within an environment. Unfortunately, computational models of grid cells are limited by the use of idealistic grid cells with uniform grid fields (Rolls et al., 2006; Solstad et al., 2006; de Almeida et al., 2009; Savelli and Knierim, 2010), even though dominant firing fields are commonly observed experimentally (Ismakov et al., 2015, Soc. Neurosci., abstract). Here, we show that the firing rates of individual grid fields were stable during repeated exposures to a familiar environment but that CNO drastically altered the rates of individual fields in an imbalanced manner *only* in hM3 mice. This observation thus provides a possible mechanism underlying artificial remapping. In fact, this inter-field variability was sufficient to decode whether the network was in a depolarized state with only a few cells, which is analogous to decoding which room the animal is in during natural remapping experiments. It is entirely conceivable that rate changes in grid fields lead to locational changes of hippocampal place fields during natural remapping as well, but it is currently impossible to track the identity of grid fields between environments as they shift and rotate. We propose that this novel mechanism maximizes the contextual information conveyed by grid cells. If it is found that different modules do not shift relative to each other in distinct environments, this would in fact be the only mechanism supported by empirical evidence to explain remapping.

If the spatial changes in MEC underlying remapping are a result of changes in the firing rates of individual grid fields, it raises the question of how this interfield variability arises. Environmental changes have been shown to locally affect properties of the grid pattern (Krupic et al., 2012, 2013, 2015; Stensola et al., 2012). In addition, interneurons have spatially nonuniform firing patterns (Buetfering et al., 2014), suggesting that changes in their activity would differentially affect individual grid fields, consistent with the results presented here. This makes examining the changes in MEC interneuron firing patterns during conditions that elicit hippocampal remapping of particular interest. Taken together, our results mechanistically link changes in grid cell activity to remapping in place cells. Grid cells are in fact able to convey distinct sets of spatial input to the hippocampus without changing their relative position, but only if individual grid fields are considered discrete spatial inputs.

STAR★METHODS

Detailed methods are provided in the online version of this paper and include the following:

- KEY RESOURCES TABLE
- CONTACT FOR REAGENT AND RESOURCE SHARING
- EXPERIMENTAL MODEL AND SUBJECT DETAILS
- METHOD DETAILS
  - Histological Procedures
  - Cell Counting
  - Water Maze
  - Surgical Procedures
  - Electrophysiology Behavioral Protocol
  - Single Unit Recording
  - Unit Isolation and Recording Stability
  - General Electrophysiological Analysis
  - Functional Classification of CA1 Cells
  - Functional Classification of MEC Cells
  - Population Vector Analysis
  - Model of Grid-to-Place Cell Transformation
  - Individual Grid Cell Firing Fields
  - Contextual Discrimination
  - Context-Specific Cells
- QUANTIFICATION AND STATISTICAL ANALYSIS
- DATA AND SOFTWARE AVAILABILITY

SUPPLEMENTAL INFORMATION

Supplemental Information includes five figures and two tables and can be found with this article online at http://dx.doi.org/10.1016/j.neuron.2017.03.001.

AUTHOR CONTRIBUTIONS

Conceptualization, C.G.K.; Methodology, C.G.K.; Software, B.R.K. and B.D.; Formal analysis, B.R.K., C.M.L., and B.D.; Investigation, A.W., D.A., J.D., C.M.L., B.R.K., and N.Z.B.; Writing – Original Draft, B.R.K., C.G.K., and C.M.L.; Writing – Review & Editing, B.R.K., C.M.L., C.G.K., N.Z.B., B.D., D.A., and J.D.; Visualization, B.R.K., C.M.L., B.D., and A.W.; Funding Acquisition, C.G.K.; Resources, C.G.K.; Supervision, C.G.K. and Y.R. (of B.D.).

ACKNOWLEDGMENTS

We thank Y. Yanovich and K. Asumbisa for help with experiments, H. Wu for in situ hybridization, and D.C. Rowland for comments on the manuscript. Supported by NIH Grant R01MH097130-05, Kavli Foundation, the Centre of Excellence scheme of the Research Council of Norway – Centre for Biology of Memory and Centre for Neural Computation, The Egil and Pauline Braathen and Fred Kavli Centre for Cortical Microcircuits, and the National Infrastructure scheme of the Research Council of Norway – NORBRAIN.

Received: September 5, 2016
Revised: December 30, 2016
Accepted: February 28, 2017
Published: March 22, 2017

REFERENCES

Alexander, G.M., Rogan, S.C., Abbas, A.I., Armbruster, B.N., Pei, Y., Allen, J.A., Nonneman, R.J., Hartmann, J., Moy, S.S., Nicolelis, M.A., et al. (2009). Remote control of neuronal activity in transgenic mice expressing evolved G protein-coupled receptors. Neuron *63*, 27–39.

Barry, C., Lever, C., Hayman, R., Hartley, T., Burton, S., O'Keefe, J., Jeffery, K., and Burgess, N. (2006). The boundary vector cell model of place cell firing and spatial memory. Rev. Neurosci. *17*, 71–97.

Barry, C., Ginzberg, L.L., O'Keefe, J., and Burgess, N. (2012). Grid cell firing patterns signal environmental novelty by expansion. Proc. Natl. Acad. Sci. USA *109*, 17687–17692.

Bjerknes, T.L., Moser, E.I., and Moser, M.B. (2014). Representation of geometric borders in the developing rat. Neuron *82*, 71–78.

Brandon, M.P., Bogaard, A.R., Libby, C.P., Connerney, M.A., Gupta, K., and Hasselmo, M.E. (2011). Reduction of theta rhythm dissociates grid cell spatial periodicity from directional tuning. Science *332*, 595–599.

Brandon, M.P., Koenig, J., Leutgeb, J.K., and Leutgeb, S. (2014). New and distinct hippocampal place codes are generated in a new environment during septal inactivation. Neuron *82*, 789–796.

Brun, V.H., Leutgeb, S., Wu, H.Q., Schwarcz, R., Witter, M.P., Moser, E.I., and Moser, M.B. (2008). Impaired spatial representation in CA1 after lesion of direct input from entorhinal cortex. Neuron *57*, 290–302.

Buetfering, C., Allen, K., and Monyer, H. (2014). Parvalbumin interneurons provide grid cell-driven recurrent inhibition in the medial entorhinal cortex. Nat. Neurosci. *17*, 710–718.

Couey, J.J., Witoelar, A., Zhang, S.J., Zheng, K., Ye, J., Dunn, B., Czajkowski, R., Moser, M.B., Moser, E.I., Roudi, Y., and Witter, M.P. (2013). Recurrent inhibitory circuitry as a mechanism for grid formation. Nat. Neurosci. *16*, 318–324.

de Almeida, L., Idiart, M., and Lisman, J.E. (2009). The input-output transformation of the hippocampal granule cells: from grid cells to place fields. J. Neurosci. *29*, 7504–7512.

Dhillon, A., and Jones, R.S. (2000). Laminar differences in recurrent excitatory transmission in the rat entorhinal cortex in vitro. Neuroscience *99*, 413–422.

Ferrante, M., Tahvildari, B., Duque, A., Hadzipasic, M., Salkoff, D., Zagha, E.W., Hasselmo, M.E., and McCormick, D.A. (2016). Distinct functional groups emerge from the intrinsic properties of molecularly identified entorhinal interneurons and principal cells. Cereb. Cortex. Published online June 6, 2016. http://dx.doi.org/10.1093/cercor/bhw143.

Fiete, I.R., Burak, Y., and Brookings, T. (2008). What grid cells convey about rat location. J. Neurosci. *28*, 6858–6871.

Fyhn, M., Molden, S., Witter, M.P., Moser, E.I., and Moser, M.B. (2004). Spatial representation in the entorhinal cortex. Science *305*, 1258–1264.

Fyhn, M., Hafting, T., Treves, A., Moser, M.B., and Moser, E.I. (2007). Hippocampal remapping and grid realignment in entorhinal cortex. Nature *446*, 190–194.

Gatome, C.W., Slomianka, L., Lipp, H.P., and Amrein, I. (2010). Number estimates of neuronal phenotypes in layer II of the medial entorhinal cortex of rat and mouse. Neuroscience *170*, 156–165.

Glorot, X., Bordes, A., and Bengio, Y. (2011). Deep sparse rectifier neural networks. J. Mach. Learn. Res. *15*, 315–323.

Gray, C.M., Maldonado, P.E., Wilson, M., and McNaughton, B. (1995). Tetrodes markedly improve the reliability and yield of multiple single-unit isolation from multi-unit recordings in cat striate cortex. J. Neurosci. Methods *63*, 43–54.

Hafting, T., Fyhn, M., Molden, S., Moser, M.B., and Moser, E.I. (2005). Microstructure of a spatial map in the entorhinal cortex. Nature *436*, 801–806.

Hales, J.B., Schlesiger, M.I., Leutgeb, J.K., Squire, L.R., Leutgeb, S., and Clark, R.E. (2014). Medial entorhinal cortex lesions only partially disrupt hippocampal place cells and hippocampus-dependent place memory. Cell Rep. *9*, 893–901.

Kentros, C.G., Agnihotri, N.T., Streater, S., Hawkins, R.D., and Kandel, E.R. (2004). Increased attention to spatial context increases both place field stability and spatial memory. Neuron *42*, 283–295.

Kitamura, T., Sun, C., Martin, J., Kitch, L.J., Schnitzer, M.J., and Tonegawa, S. (2015). Entorhinal cortical ocean cells encode specific contexts and drive context-specific fear memory. Neuron *87*, 1317–1331.

Koenig, J., Linder, A.N., Leutgeb, J.K., and Leutgeb, S. (2011). The spatial periodicity of grid cells is not sustained during reduced theta oscillations. Science *332*, 592–595.

Köhler, C. (1985). Intrinsic projections of the retrohippocampal region in the rat brain. I. The subicular complex. J. Comp. Neurol. *236*, 504–522.

Kropff, E., Carmichael, J.E., Moser, M.B., and Moser, E.I. (2015). Speed cells in the medial entorhinal cortex. Nature *523*, 419–424.

Krupic, J., Burgess, N., and O'Keefe, J. (2012). Neural representations of location composed of spatially periodic bands. Science *337*, 853–857.

Krupic, J., Bauza, M., Burton, S., Lever, C., and O'Keefe, J. (2013). How environment geometry affects grid cell symmetry and what we can learn from it. Philos. Trans. R. Soc. Lond. B Biol. Sci. *369*, 20130188.

Krupic, J., Bauza, M., Burton, S., Barry, C., and O'Keefe, J. (2015). Grid cell symmetry is shaped by environmental geometry. Nature *518*, 232–235.

Langston, R.F., Ainge, J.A., Couey, J.J., Canto, C.B., Bjerknes, T.L., Witter, M.P., Moser, E.I., and Moser, M.B. (2010). Development of the spatial representation system in the rat. Science *328*, 1576–1580.

Leutgeb, S., Leutgeb, J.K., Barnes, C.A., Moser, E.I., McNaughton, B.L., and Moser, M.B. (2005). Independent codes for spatial and episodic memory in hippocampal neuronal ensembles. Science *309*, 619–623.

Lykken, C., and Kentros, C.G. (2014). Beyond the bolus: transgenic tools for investigating the neurophysiology of learning and memory. Learn. Mem. *21*, 506–518.

Mathis, A., Herz, A.V., and Stemmler, M. (2012). Optimal population codes for space: grid cells outperform place cells. Neural Comput. *24*, 2280–2317.

Miao, C., Cao, Q., Ito, H.T., Yamahachi, H., Witter, M.P., Moser, M.B., and Moser, E.I. (2015). Hippocampal remapping after partial inactivation of the medial entorhinal cortex. Neuron *88*, 590–603.

Miettinen, M., Koivisto, E., Riekkinen, P., and Miettinen, R. (1996). Coexistence of parvalbumin and GABA in nonpyramidal neurons of the rat entorhinal cortex. Brain Res. *706*, 113–122.

Miller, V.M., and Best, P.J. (1980). Spatial correlates of hippocampal unit activity are altered by lesions of the fornix and endorhinal cortex. Brain Res. *194*, 311–323.

Monaco, J.D., and Abbott, L.F. (2011). Modular realignment of entorhinal grid cell activity as a basis for hippocampal remapping. J. Neurosci. *31*, 9414–9425.

Muller, R.U., and Kubie, J.L. (1987). The effects of changes in the environment on the spatial firing of hippocampal complex-spike cells. J. Neurosci. *7*, 1951–1968.

Muller, R.U., and Kubie, J.L. (1989). The firing of hippocampal place cells predicts the future position of freely moving rats. J. Neurosci. *9*, 4101–4110.

O'Keefe, J., and Dostrovsky, J. (1971). The hippocampus as a spatial map. Preliminary evidence from unit activity in the freely-moving rat. Brain Res. *34*, 171–175.

Ormond, J., and McNaughton, B.L. (2015). Place field expansion after focal MEC inactivations is consistent with loss of Fourier components and path integrator gain reduction. Proc. Natl. Acad. Sci. USA *112*, 4116–4121.

Parron, C., Poucet, B., and Save, E. (2004). Entorhinal cortex lesions impair the use of distal but not proximal landmarks during place navigation in the rat. Behav. Brain Res. *154*, 345–352.

Pastoll, H., Solanka, L., van Rossum, M.C., and Nolan, M.F. (2013). Feedback inhibition enables θ-nested γ oscillations and grid firing fields. Neuron *77*, 141–154.

Pérez-Escobar, J.A., Kornienko, O., Latuske, P., Kohler, L., and Allen, K. (2016). Visual landmarks sharpen grid cell metric and confer context specificity to neurons of the medial entorhinal cortex. eLife *5*, 5.

Rolls, E.T., Stringer, S.M., and Elliot, T. (2006). Entorhinal cortex grid cells can map to hippocampal place cells by competitive learning. Network *17*, 447–465.

Rowland, D.C., Weible, A.P., Wickersham, I.R., Wu, H., Mayford, M., Witter, M.P., and Kentros, C.G. (2013). Transgenically targeted rabies virus demonstrates a major monosynaptic projection from hippocampal area CA2 to medial entorhinal layer II neurons. J. Neurosci. *33*, 14889–14898.

Rueckemann, J.W., DiMauro, A.J., Rangel, L.M., Han, X., Boyden, E.S., and Eichenbaum, H. (2016). Transient optogenetic inactivation of the medial entorhinal cortex biases the active population of hippocampal neurons. Hippocampus *26*, 246–260.

Sargolini, F., Fyhn, M., Hafting, T., McNaughton, B.L., Witter, M.P., Moser, M.B., and Moser, E.I. (2006). Conjunctive representation of position, direction, and velocity in entorhinal cortex. Science *312*, 758–762.

Savelli, F., and Knierim, J.J. (2010). Hebbian analysis of the transformation of medial entorhinal grid-cell inputs to hippocampal place fields. J. Neurophysiol. *103*, 3167–3183.

Schlesiger, M.I., Cannova, C.C., Boublil, B.L., Hales, J.B., Mankin, E.A., Brandon, M.P., Leutgeb, J.K., Leibold, C., and Leutgeb, S. (2015). The medial entorhinal cortex is necessary for temporal organization of hippocampal neuronal activity. Nat. Neurosci. *18*, 1123–1132.

Skaggs, W.E., McNaughton, B.L., Wilson, M.A., and Barnes, C.A. (1996). Theta phase precession in hippocampal neuronal populations and the compression of temporal sequences. Hippocampus *6*, 149–172.

Solstad, T., Moser, E.I., and Einevoll, G.T. (2006). From grid cells to place cells: a mathematical model. Hippocampus *16*, 1026–1031.

Sreenivasan, S., and Fiete, I. (2011). Grid cells generate an analog error-correcting code for singularly precise neural computation. Nat. Neurosci. *14*, 1330–1337.

Steffenach, H.A., Witter, M., Moser, M.B., and Moser, E.I. (2005). Spatial memory in the rat requires the dorsolateral band of the entorhinal cortex. Neuron *45*, 301–313.

Stemmler, M., Mathis, A., and Herz, A.V. (2015). Connecting multiple spatial scales to decode the population activity of grid cells. Sci. Adv. *1*, e1500816.

Stensola, H., Stensola, T., Solstad, T., Frøland, K., Moser, M.B., and Moser, E.I. (2012). The entorhinal grid map is discretized. Nature *492*, 72–78.

Taube, J.S., Muller, R.U., and Ranck, J.B., Jr. (1990). Head-direction cells recorded from the postsubiculum in freely moving rats. II. Effects of environmental manipulations. J. Neurosci. *10*, 436–447.

Van Cauter, T., Poucet, B., and Save, E. (2008). Unstable CA1 place cell representation in rats with entorhinal cortex lesions. Eur. J. Neurosci. *27*, 1933–1946.

Vorhees, C.V., and Williams, M.T. (2006). Morris water maze: procedures for assessing spatial and related forms of learning and memory. Nat. Protoc. *1*, 848–858.

Wills, T.J., Cacucci, F., Burgess, N., and O'Keefe, J. (2010). Development of the hippocampal cognitive map in preweanling rats. Science *328*, 1573–1576.

Wilson, M.A., and McNaughton, B.L. (1993). Dynamics of the hippocampal ensemble code for space. Science *261*, 1055–1058.

Wouterlood, F.G., Härtig, W., Brückner, G., and Witter, M.P. (1995). Parvalbumin-immunoreactive neurons in the entorhinal cortex of the rat: localization, morphology, connectivity and ultrastructure. J. Neurocytol. *24*, 135–153.

Yasuda, M., and Mayford, M.R. (2006). CaMKII activation in the entorhinal cortex disrupts previously encoded spatial memory. Neuron *50*, 309–318.

Yetman, M.J., Lillehaug, S., Bjaalie, J.G., Leergaard, T.B., and Jankowsky, J.L. (2016). Transgene expression in the Nop-tTA driver line is not inherently restricted to the entorhinal cortex. Brain Struct. Funct. *221*, 2231–2249.

Zhang, S.J., Ye, J., Miao, C., Tsao, A., Cerniauskas, I., Ledergerber, D., Moser, M.B., and Moser, E.I. (2013). Optogenetic dissection of entorhinal-hippocampal functional connectivity. Science *340*, 1232627.

Zhao, R., Grunke, S.D., Keralapurath, M.M., Yetman, M.J., Lam, A., Lee, T.C., Sousounis, K., Jiang, Y., Swing, D.A., Tessarollo, L., et al. (2016). Impaired recall of positional memory following chemogenetic disruption of place field stability. Cell Rep. *16*, 793–804.

STAR★METHODS

KEY RESOURCES TABLE

REAGENT or RESOURCE	SOURCE	IDENTIFIER
Antibodies		
Rabbit anti-HA	Rockland	Code: 600-401-384; RRID: AB_217929
Fluor 488 Goat anti-rabbit IgG	Thermo Fisher Scientific	SKU: A-11008; RRID: AB_143165
Chemicals, Peptides, and Recombinant Proteins		
Clozapine N-oxide	Sigma-Aldrich	SKU: C0832; CAS Number: 34233-97-7; MDL Number: MFCD00210190; PubChem Substance ID: 24892276
Experimental Models: Organisms/Strains		
Mouse: C57BL/6J	The Jackson Laboratory	Stock: 000644; RRID: IMSR_JAX:000664
Mouse: B6.Cg-Tg(Klk8-tTA)SMmay/MullMmmh	Mutant Mouse Resource & Research Centers	Stock: 031779-MU; RRID: MMRRC_031779-MU
Mouse: Tg(tetO-CHRM3*)1Blr/J	The Jackson Laboratory	Stock: 014093; RRID: IMSR_JAX:014093
Mouse: Tg(tetO-CHRM4*)2Blr/J	The Jackson Laboratory	Stock: 024114; RRID: IMSR_JAX:024114
Software and Algorithms		
MetaMorph Premier	Molecular Devices	https://www.moleculardevices.com/systems/metamorph-research-imaging/metamorph-microscopy-automation-and-image-analysis-software
Photoshop CS4	Adobe Systems	http://www.adobe.com/products/photoshop.html
Image Pro Plus	Media Cybernetics	http://www.mediacy.com/imageproplus
AnyMaze	Stoelting	http://www.stoeltingco.com/anymaze.html
Cheetah	Neuralynx	http://neuralynx.com/research_software/cheetah
MATLAB	MathWorks	https://se.mathworks.com/products/matlab.html
MClust	Redish et al.	http://redishlab.neuroscience.umn.edu/MClust/MClust.html
Python	Python	https://www.python.org/

CONTACT FOR REAGENT AND RESOURCE SHARING

Further information and requests for resources and reagents should be directed to and will be fulfilled by the Lead Contact Dr. Clifford Kentros (clifford.kentros@ntnu.no).

EXPERIMENTAL MODEL AND SUBJECT DETAILS

Our subjects were adult (2 - 6 months, 17 – 37 g) male and female mice. We crossed the EC-tTA line (Mutant Mouse Resource & Research Centers, Stock: 031779-MU; RRID: MMRRC_031779-MU) to hM3Dq- and hM4Di-tetO lines (Jackson Laboratory, Stock: 014093 & 024114; RRID: IMSR_JAX:014093 & RRID: IMSR_JAX:024114) to enable control of neurons in the superficial layers of medial entorhinal cortex. Pups were evaluated for transgenic expression via PCR of genomic DNA isolated from tail biopsies. We also used C57BL/6J (Jackson Laboratory, Stock: 000644; RRID: IMSR_JAX:000664) mice as an additional control group. Mice were kept on a 12-hr light/dark schedule and were fed ad libitum. They were housed in environmentally-enriched transparent Plexiglas cages in a humidity- and temperature-controlled environment. Mice were group-housed prior to surgery or water maze testing and then housed separately. Mice were experimentally-naive before surgery or water maze testing, and were randomly assigned to experimental groups when applicable. All procedures were approved by the Institutional Animal Care and Use Committee at the University of Oregon and the National Animal Research Authorities of Norway. They were performed according to the Norwegian Animal Welfare Act and the European Convention for the Protection of Vertebrate Animals used for Experimental and Other Scientific Purposes.

METHOD DETAILS

Histological Procedures

For HA-antibody labeling, air-dried slides were first washed in 1X phosphate-buffered saline (PBS) (3 × 10 min). Sections were then blocked with 5% NDS (normal donkey serum) in PBT (0.3% Triton in 1X PBS). Slides were placed on a flat staining rack and covered with 0.3 mL blocking solution for 20 min at room temperature. We prepared the primary antibody (rabbit anti-HA; Rockland, Code: 600-401-384; RRID: AB_217929; 1:500 dilution) in a solution of 5% NDS in PBT supplemented with 0.1% NaN3 for extended stabilization. Each section was bathed with 250 μl of the antibody solution, and the slide covered with Parafilm™ and stored overnight at 4°C. We prepared the secondary antibody (Fluor 488 Goat anti-rabbit IgG; Thermo Fisher Scientific, SKU: A-11008; RRID: AB_143165) in PBT. The day following primary antibody processing, sections were washed in PBT (4 × 10 min). Each section was bathed with 250 μl of the secondary solution, covered in Parafilm, wrapped in foil and stored overnight at 4°C. A final wash was then performed with PBT (4 × 10 min) and then 1X PBS (5 min). Slides were then coverslipped and stored at 4°C.

When electrophysiological recordings were complete, mice were anaesthetized with isoflurane and each tetrode was electrolytically lesioned (5 V, 500 ms) for identification. After 24-48 hr, mice were administered a lethal dose of pentobarbital sodium (Euthasol, 50mg/kg) and perfused transcardially with 4% paraformaldehyde in phosphate-buffered saline (PBS). Brains were removed and post-fixed in paraformaldehyde overnight, then transferred to a 30% sucrose solution. Brains were sectioned (30 μm) in the sagittal plane and mounted on glass microscope slides. Slides were air-dried overnight and then processed or stored at −80°C. For identification of recording sites, the tissue was stained with either Cresyl violet or VECTASHIELD Antifade Mounting Medium with DAPI (Vector Laboratories, Inc., Burlingame, CA). The slides were then coverslipped and examined under the microscope. Recording sites were marked on copies of the Paxinos and Franklin atlas (2008) and slides were stored at room temperature.

Cell Counting

Tissue was analyzed from nine mice, counting cells from each region in as many different sections as possible, which ranged from one to three sections. Scans of histochemical RNA in situ and fluorescent Nissls were acquired at 10X magnification and stitched together in MetaMorph Premier (Molecular Devices, CA) using the following equipment: Olympus BX61 microscope, DP72 camera, BX-UCB control box, Prior ProScanIII motorized stage, and Lumen200Pro light source. The scanned files were then saved as jpegs. In situ and Nissl images were analyzed separately to obtain the number of transgenic neurons in each structure and the total number of cells in each structure, respectively. Anatomical regions were delineated using the Paxinos and Franklin sagittal atlas (2008) as a reference, with known anatomical landmarks such as lamina dissecans used to determine the local extent and layers of MEC. The total number of cells in each structure was estimated in Photoshop CS4 (Adobe Systems, CA) using a hole punch technique. A circular outline of fixed area was placed in a region of each structure that was most representative of its overall cell density. All nuclei within this hole punch region were counted. To obtain the total number of cells in each structure, the area of the hole punch was determined by calculating the number of pixels inside the hole punch. The same strategy was used to determine the area of each structure. The area of each structure was then divided by the area of the hole punch and the resulting number was multiplied by the number of cells in that structure. These estimates were then used to obtain the percent of total cells (i.e., nuclei) in each structure that were transgenic.

Water Maze

51 experimentally-naive, unimplanted mice (13 hM3+, 9 hM3-, 13 hM4+, 16 hM4-) were housed in littermate pairs for the duration of water maze training. The control group included single and double negative littermates. All training and tests were performed during the light cycle in a 104 cm diameter pool maintained at 28°C. The water was made opaque with white Tempera paint (Beaverton, OR). We employed a behavioral protocol adapted from Voorhees and colleagues (Vorhees and Williams, 2006). Mice were given one training session consisting of four trials per day for a total of eight days, followed by two days of single probe tests. Each trial was 60 s in duration, or until the mouse remained on the platform for 15 s. Mice that climbed onto the platform but jumped off before 15 s elapsed were guided back to the platform. The inter-trial interval was approximately 120 s. For each trial, the mouse started from a pseudorandom start location, selected from the eight cardinal and intercardinal positions relative to the platform, excluding the location of the platform and those immediately adjacent (i.e., if the platform was at location N, the mouse could start from W, SW, S, SE, or E, but not NW, N, or NE). No start position was used more than once during a single session. During the first two days of training (Days 1 & 2), a wire mesh cup was set atop the 10 × 10 cm platform submerged 1 cm beneath the surface. These visually cued trials were performed to test the mouse's ability to swim to a visible goal. Day 3 was the first of six daily submerged platform spatial acquisition sessions (Days 3-8). Acquisition of the task relied on the use of distal cues beyond the walls of the pool. On Days 9 and 10, mice were given a single probe test during which the platform was absent. On each day, each mouse was placed in the pool at the same pseudorandomly selected start position for that day (following the same rules above), allowed to swim for 60 s, and was then removed. Start positions were not the same on Days 9 and 10. 30 min prior to the first probe trial (Day 9), all mice were injected with CNO as described below. 30 min prior to the second probe trial (Day 10), all mice were injected with saline. All sessions were recorded with a Sony Handycam DCR-HC42 extended on a boom directly over the pool. Swimming behavior was tracked automatically using either Image Pro Plus (Bethesda, MD) or AnyMaze (Stoelting Co, Kiel, WI). The target location was defined as a region with a radius 6 cm from the center of the platform location. Test results were exported to MATLAB for statistical testing and visualization.

Surgical Procedures

All surgeries were performed using aseptic techniques on experimentally-naive mice. Prior to surgical implantation of the microdrives, ketamine (100 mg/kg) was administered as a preanesthetic. Dexamethasone (0.1 mg/kg) and atropine (0.03 mg/kg) were also administered presurgically to ameliorate possible inflammation and respiratory irregularities, respectively. Surgical anesthesia was maintained with isoflurane (1.25%–2.0%, adjusted as necessary for appropriate depth of anesthesia). Eyes were moistened with antibacterial ophthalmic ointment. Mice were placed in a stereotaxic frame and held in position with atraumatic ear bars. The skull was exposed and lambda and bregma were zeroed in the vertical plane. The surface of the skull was cleaned with hydrogen peroxide, lightly scored with a dental pick, and coated with a thin layer of cyanoacrylate glue that was allowed to dry completely before proceeding. For recordings from CA1, one craniotomy was drilled in the left hemisphere overlying the dorsal hippocampus (centered at AP: −1.8 mm; ML: 1.2 mm relative to bregma). For recordings from medial entorhinal cortex (MEC), one craniotomy was drilled in the left hemisphere, exposing the transverse sinus 3.2 mm lateral to the midline. Four additional holes were drilled around the perimeter of the skull for stainless steel anchor screws (00–90 × 1/8") and ground wires from the recording array. The tetrodes of the array were lowered into the cortex overlying the hippocampus or MEC to a depth of approximately 0.8 mm. In MEC, the tetrode array was implanted 300-500 μm anterior of the transverse sinus at a 3 - 6 degree angle aimed posteriorly. Grip Cement (Dentsply, Milford, DE) was applied to secure the array to the skull. After the implant was in place, sterile Vaseline was applied to isolate the tetrodes from the cement, preserving the ability to adjust tetrode depth. Mice were subcutaneously administered buprenorphine (0.06 mg/kg) postoperatively for analgesia to minimize discomfort.

Electrophysiology Behavioral Protocol

All implanted mice were allowed to recover from surgery for seven days, after which screening for units began. A tethered HS-16 or HS-18MM operational amplifier (Neuralynx, Bozeman, MT) was plugged into the tetrode recording array to monitor/record behavior and neuronal activity. Recording sessions occurred based on the presence of neural activity, regardless of the light/dark cycle. All MEC screening and recording sessions were performed in a cue-rich room in either a 90 × 120 cm rectangular environment or a 100 × 100 cm square environment. Each mouse experienced only one environment. All hippocampal screening and recording sessions were performed in a 60 cm diameter cylinder with dominant visual cues. During initial screening sessions, the array was moved down 45-90 μm per day, and an audio channel was monitored for evidence of theta rhythmicity and/or the occurrence of sharp waves. Recordings of MEC activity were initiated when cells with clear spatial or head direction correlates were first observed. Recordings of hippocampal activity were initiated when spiking activity with clear spatial correlates was first observed. Baseline activity was recorded for 30 min. Mice were then removed from the cylinder and given an intraperitoneal injection of either clozapine N-oxide (CNO, Sigma-Aldrich, St. Louis, Missouri, USA) (hM3: 1 mg/kg, 0.1 mg/ml in 10% DMSO/saline solution; hM4: 10 mg/kg, 1.0 mg/ml in 10% DMSO/saline solution) or saline. Immediately following the injection, mice were placed back into the environment and data were recorded for an additional 120 min. Mice were then removed from the environment, placed in their home cages, and returned to the colony room. When recording from the hippocampus, mice were returned to the cylinder for a second 30 min baseline session after a 12-24 hr delay. Experiments were repeated for each mouse as long as activity was present. The hippocampal and MEC control groups include hM3 and hM4 mice injected with saline, and littermate controls injected with either CNO or saline. The MEC control group also includes C57BL/6J mice injected with CNO when the data from this group was indistinguishable from that of the controls (two-sample Kolmorogov-Smirnov test, $p > 0.05$).

Single Unit Recording

Tetrodes were made by spinning together four lengths of 18-micron-diameter 10% iridium/platinum wire (California Fine Wire, Grover Beach, CA) and applying heat to fuse the polyamide coating at one end. The majority of experiments used custom-made four-tetrode recording arrays adapted from methods described by Gray et al. (1995). The coating on the free ends of each wire was removed and each uncoated wire segment was inserted into a channel of an EIB-16 electrode interface board (Neuralynx) and fixed in place with a gold-coated pin. Each EIB-16 loaded with four tetrodes was fixed to a Teflon stage mounted on three drive screws. The drive screws (0–80 × 3/8") allowed depth adjustments of the entire array and served as a structural link to the skull. The remaining experiments used VersaDrive-4 microdrives (Neuralynx), where the tetrodes could each be lowered independently. Neuronal data were acquired using the Cheetah-16 system (Neuralynx). Recorded signals were amplified automatically for each tetrode when the experimenter selected an appropriate input range (typically ± 250-800 μV). The signals were band-pass filtered (spikes: 600 – 6000 Hz; local field potential: 0.1 – 475 Hz) and stored using Neuralynx data-acquisition software. Thresholds were set such that only waveforms of a specified minimum voltage (e.g., 50 μV) were stored. A digital camera mounted above the recording environment and linked to the Cheetah-16 system recorded the position of the mouse by tracking two light-emitting diodes fixed to the headstage and aligned with the body axis of the mouse.

Unit Isolation and Recording Stability

Unit isolation and assessment of recording stability was performed on a total of five distinct 30 min epochs for MEC recordings, including the baseline session (BL) and the 2 hr post-injection session, which was divided into four 30 min epochs for analysis purposes. For CA1 recordings, a final 30 min session a minimum of 12 hr after injection (12+ hr) was included as well. Units were manually separated offline with MClust spike-sorting software (courtesy of David Redish, University of Minnesota) for MATLAB (MathWorks,

Natick, MA) using the strict standards for unit isolation described previously by Kentros et al. (2004), and cluster boundaries were applied across successive sessions to track clusters over time. Isolated clusters corresponding to putative pyramidal neurons formed clear Gaussian ellipses generally based upon peak-to-peak projections of different tetrode wires with minimal overlap with neighboring clusters or noise. These clusters were divided into one of three groups according to a subjective judgment of quality (Q). Q-1 clusters had virtually no overlap on at least one projection and no events within a 2 ms refractory period; Q-2 clusters included clear Gaussians with a small degree of overlap with other clusters or noise; Q-3 cells met neither criteria; Q-off cells did not have enough spikes to judge the quality. Neurons categorized as Q-3 were not included for any analyses. Putative interneurons with generally spherical clusters were assigned Q-values exclusively by cluster boundary criteria. Cluster boundaries were then applied across successive epochs and minor adjustments were made when necessary to optimally separate clusters from each other and from noise. Inspection of spike waveforms, inter-spike intervals, autocorrelations, and cross-correlations were used as additional methods to ensure each cluster was correctly tracked over time. In two-session comparisons (i.e., spatial correlations), it was required that clusters in both sessions passed criteria to be included. In CA1, we recorded 810 cells from 23 mice (7 hM3+, 4 hM3-, 11 hM4+, 1 hM4-). 672 of those cells (83%) met our standards of cluster quality. In MEC, we recorded 383 cells from 17 mice (7 hM3+, 1 hM3-, 5 hM4+, 4 C57BL/6J). 297 of those cells (76%) met our standards of cluster quality.

General Electrophysiological Analysis

Unless otherwise indicated, only the 30-60 min epoch of the 2 hr post-injection recording session was included in the analysis. This epoch was chosen because it captures the peak activity of CNO. The first 30 min included considerable time when CNO was not active, and the last hour was redundant as firing properties did not continue to significantly change after 60 min (Figure S4). Furthermore, it allowed for the comparison of sessions that are equal in length which is more statistically appropriate.

In order to exclude spiking activity occurring during periods of immobility, a walk filter ($\geq$2 cm/s) was applied. Rate maps were then generated by binning the location of each spike (CA1: 2 × 2 cm bins; MEC: 4 × 4 cm bins) for each 30 min epoch, dividing the number of spikes in each bin by the time spent in that bin, and smoothing with a Gaussian. Mean firing rate was defined as the total number of spikes divided by the duration of the recording session. Peak firing rate was defined as the maximal firing rate of all spatial bins. To assess spatial correlation, pairs of rate maps were each reshaped into a single vector and the correlation coefficient (Pearson's linear correlation) between these vectors was calculated. Pixels of incongruity between the two vectors, resulting from unvisited pixels in either epoch, were excluded from the calculation. Example rate maps from hM4 mice in Figures 5F and 7A–7C are displayed using 30-120 min post-CNO injection due to partial coverage during the 30-60 min epoch.

Difference scores were calculated as: (session 2 value – session 1 value) / (session 2 value + session 1 value), i.e., normalized change. These scores are reported in Figures 3A, 3B, 6A, 6B, 6D, 8C, and S5D, as well as in Tables S1 and S2.

Functional Classification of CA1 Cells

For the functional classification of cells, chance levels were estimated using a shuffling procedure. For each cell, its spikes were circularly shifted in time relative to the mouse's position by a random amount between 20 s and 20 s less than the total length of the recording session. The measure of interest was calculated using these shuffled spike times, and this procedure was repeated 500 times for that cell. A distribution of values was generated including the 500 shuffled results from all cells, and the 95th percentile was calculated. Cells were required to meet all defined criteria in either the baseline or the CNO session to be included.

Place cells were defined as putative excitatory neurons (mean firing rate $\leq$ 7 Hz) with good spatial stability in the baseline session (spatial correlation between first and second halves > 0.5), a mean rate $\geq$ 0.1 Hz, and at least one identified place field. Place fields were defined as areas with at least 20 contiguous pixels (80 cm^2) where the firing rate exceeded 20% of the peak rate. Place fields with peak rates lower than 1 Hz were ignored. In-field firing rate was defined as the mean firing rate within the largest place field. Coherence was calculated as the correlation between firing rate in a given spatial bin with the firing rate in its 8 neighboring spatial bins (Muller and Kubie, 1989). Spatial information content was calculated as:

$$\text{information content} = \sum_i p_i \frac{\lambda_i}{\lambda} \log_2 \frac{\lambda_i}{\lambda}$$

where p_i is the probability of the mouse being in the i-th bin (occupancy / total time), λ is the overall mean firing rate, and λ_i is the mean firing rate in the i-th bin (Skaggs et al., 1996).

A place cell was classified as turning on if mean rate > 0.1 Hz and a place field was detected in the CNO session, but mean rate < 0.1 Hz in the baseline session. The converse criteria were used to classify a place cell as turning off. For all other classifications, place cells were required to meet all criteria described in the preceding paragraph in both the baseline and CNO sessions. We evaluated changes in spatial correlation using a shuffling procedure where each cell's baseline rate map was compared to the CNO rate map of a different cell. This procedure was repeated 500 times per place cell to create a shuffled distribution of correlation scores. Place cells with spatial correlation scores less than one standard deviation above the mean of this shuffled distribution were said to have significant shifts in location. Cells that did not exhibit significant shifts in place field location and had absolute mean firing rate difference scores or mean field size difference scores greater than 0.33 were said to have significant changes in firing rate and/or field size.

Functional Classification of MEC Cells

In MEC, chance levels were estimated using a shuffling procedure in the exact manner described above for CA1 cells. Cells with a mean firing rate $\geq$ 10 Hz were classified as putative interneurons (Fyhn et al., 2004). Firing fields for putative excitatory cells were defined as areas with at least 5 contiguous pixels (80 cm^2) where the firing rate exceeded 20% of the peak rate. Firing fields with peak rates lower than 1 Hz were ignored. For analysis of individual grid fields, the firing rate threshold was increased to 35% of the peak firing rate and firing fields with peak rates lower than 0.1 Hz were ignored to optimize grid field detection.

Grid cells were identified by calculating a spatial autocorrelation map for each unsmoothed rate map (Sargolini et al., 2006). A cell's spatial periodicity was determined by comparing a central circular region of the autocorrelogram, excluding the central peak, with versions of this region rotated at 30 degree increments (Sargolini et al., 2006; Langston et al., 2010). Pearson correlations were calculated by comparing the circular region to all rotated versions. 60 and 120 degree rotations should have high correlation scores due to the triangular pattern of the grid, whereas 30, 90, and 150 degree rotations should result in low correlations. Therefore, a cell's grid score was defined as the minimum difference between correlation scores for either rotation from the first group and any rotation in the second group (range: -2 to 2). Cells with scores exceeding the 95th percentile of the shuffled distribution were classified as grid cells. Grid scale was defined as the mean center-center distance from the central grid field in the autocorrelogram to the neighboring fields. Grid rotation was defined as the change in orientation (measured in degrees) between the central grid field in the autocorrelogram and the neighboring fields. Grid shift (or translation) was defined as the distance from the center of the cross-correlogram to the center of the nearest field. Grid rotation and shift in Table S2 are defined as the minimum change between the baseline session and any 30 min CNO epoch.

Border cells were identified by calculating the difference between the maximal length of a wall touching any defined firing field and the average distance of that field from the nearest wall (Bjerknes et al., 2014). This value was normalized by dividing by the sum of the same two values such that border scores ranged from –1 to 1; a score of 1 indicates firing exclusively along the entire length of a wall. Cells with scores exceeding the 95th percentile of the shuffled distribution were classified as border cells.

Head direction cells were identified by plotting firing rate as a function of the mouse's directional heading. Tuning maps were then divided into 6 degree directional bins and the mean vector length of the circular distribution was calculated. Cells with mean vector lengths exceeding the 95th percentile of the shuffled distribution were classified as head direction cells.

Speed scores were defined as the pairwise correlation between firing rate and the mouse's speed (Kropff et al., 2015). Cells with scores exceeding the 95th percentile of the shuffled distribution were classified as speed cells.

Population Vector Analysis

Population vectors (Leutgeb et al., 2005) were calculated in the same manner for CA1 and MEC cells. Every rate map for each recording session was stacked into a three-dimensional matrix such that each *x-y* location contains firing rate information for the entire population. Population vector correlations are then simply Pearson correlations for each *x-y* location between two different recording sessions, yielding a two-dimensional matrix of correlation scores. The baseline session was used for the functional classification of cells.

Model of Grid-to-Place Cell Transformation

A rate difference score was calculated for each recorded grid cell to create a range of scores. These empirically-determined firing rate changes were then applied to a linear summation model of the grid-to-place cell transformation (Solstad et al., 2006). Briefly, the model is a two-layer network where place fields are created by linear summation of weighted inputs from grid cells. The simulation was run with the following parameters: arena size = 100 × 100 cm, bin size = 1 cm, field rate threshold = 20%, minimum field size = 12 cm, grid spacing sampled logarithmically from 28 to 73 cm, number of grid cells = 50, phase jitter = 30%. The simulation was then repeated with the exact same grid cells, but the firing rates of 20% (matched to percentage of transgene expression) of the grid cells were altered to reflect our experimental data. Each cell was multiplied by a random number drawn from the range of rate difference scores mentioned above. We then calculated the spatial correlation between each place cell from the first simulation to the second simulation with altered firing rates.

Individual Grid Cell Firing Fields

Individual grid field firing rates were defined as the peak rate of each firing field, and fields were numbered in Figure 8A according to their peak rate in the baseline session. Grid field rate correlations in Figure 8B were obtained by fitting a line between points representing the peak field rates in two epochs (BL versus CNO, or BL 1st versus 2nd half). The R^2 value (coefficient of determination) is reported for each fit. (Note: One point not shown in the bottom panel for better visualization, but included for all calculations. BL versus CNO: 34 Hz versus 29 Hz.) In Figure 8C, grid field firing rate variability is defined as the variance between the rate difference scores computed for each identified grid field of a given grid cell. Thus, a grid cell with four firing fields would have four rate difference scores, and the variability between them would be plotted as a single point in Figure 8C. The baseline session was used for the functional classification of grid cells for field analyses.

Contextual Discrimination

Rate maps for each grid cell were exported from MATLAB to Python (Python Software Foundation, https://www.python.org/) and normalized to have firing rates between 0 and 1 for the following analysis. Population vectors were then constructed for three recording epochs: baseline (BL), 30-60 min post-CNO injection (CNO1), and 60-90 min post-CNO injection (CNO2). CNO1 was compared to BL and CNO2 by computing the Euclidean distance between the firing rates for each spatial bin. The decoding performance was defined as the fraction of bins for which the distance to CNO2 was closer than the distance to BL. That is, a decoding performance value of 1 indicates that the firing rate of every spatial bin was more similar between CNO1 and CNO2 than it was between BL and CNO1. A decoding value of 0.5 is equal to chance level performance and indicates that the firing rates in half of the spatial bins were more similar to BL, and the other half of the spatial bins were more similar to CNO2. Decoding scores were calculated for increasing numbers of grid cells for both hM3 and control groups. For each number of grid cells along the x axis in Figure 8D, grid cells were randomly selected with replacement from the pool of all recorded grid cells. This procedure was repeated 1000 times and the mean and standard deviation are shown.

Context-Specific Cells

Kitamura et al. (2015) used in vivo calcium imaging to monitor the activity of MEC cells as mice explored two distinct environmental contexts. The authors assessed context-specificity of MEC cells by calculating a rate difference index for each cell: $(X - Y) / (X + Y)$, where X and Y represent the number of calcium events detected in contexts X and Y, respectively. Only cells with > 10 events during a 5 min exposure to one context were included. Scores were first calculated for repeated exposures to the same context, and the 99^{th} percentile of these scores (0.6) was used as a threshold for classifying cells as ''context-specific.''

While data from calcium imaging experiments cannot be directly compared with the electrophysiological data reported here, we nonetheless attempted to create an analogous measure. We computed rate difference scores (defined above) for all cells and included only those cells with a mean firing rate > 0.1 Hz in either the baseline or CNO session. Our threshold for context-specificity was defined by calculating the 99^{th} percentile of scores for littermate control mice before and after CNO injection (0.85).

QUANTIFICATION AND STATISTICAL ANALYSIS

Unless otherwise noted, all analyses were conducted using MATLAB (MathWorks). The experimenter was blind to the mouse's genotype and experimental grouping during analysis. Two-sided statistical tests were used for post hoc analyses and one-sided tests were used when there was a clear a priori prediction. Statistical significance was defined with alpha level = 0.05. Nonparametric tests were used when the assumptions for parametric tests were clearly violated (Lilliefors normality test). Median values are reported/displayed for nonparametric tests and mean values are reported/displayed for parametric tests. Error is always reported as standard error of the mean (SEM) with the exception of Figure 8D where standard deviation is reported. N represents the number of mice for cell counting and water maze behavior. N represents the number of spatial bins for population vectors in Figures 7D–7E, and Tables S1 and S2. N represents the number of grid cell firing fields in Figure 8B. In all other instances, n represents the number of cells. N is reported in the Results section and in Tables S1 and S2 with the exception of the cell counts, where it is reported in the legend for Figure 1C.

DATA AND SOFTWARE AVAILABILITY

All quantification methods used in the custom scripts are described above. Further requests for custom scripts and data used in this study should be directed to the corresponding author (clifford.kentros@ntnu.no).

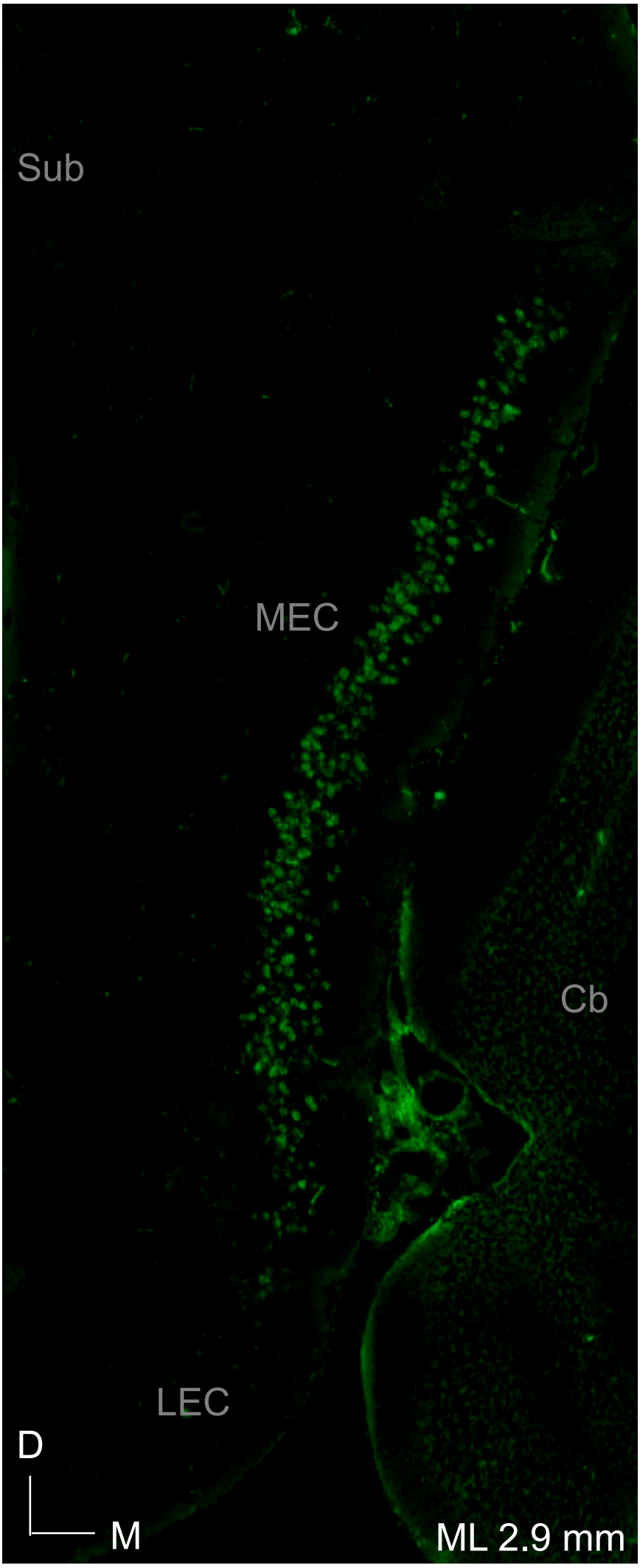

Figure S1

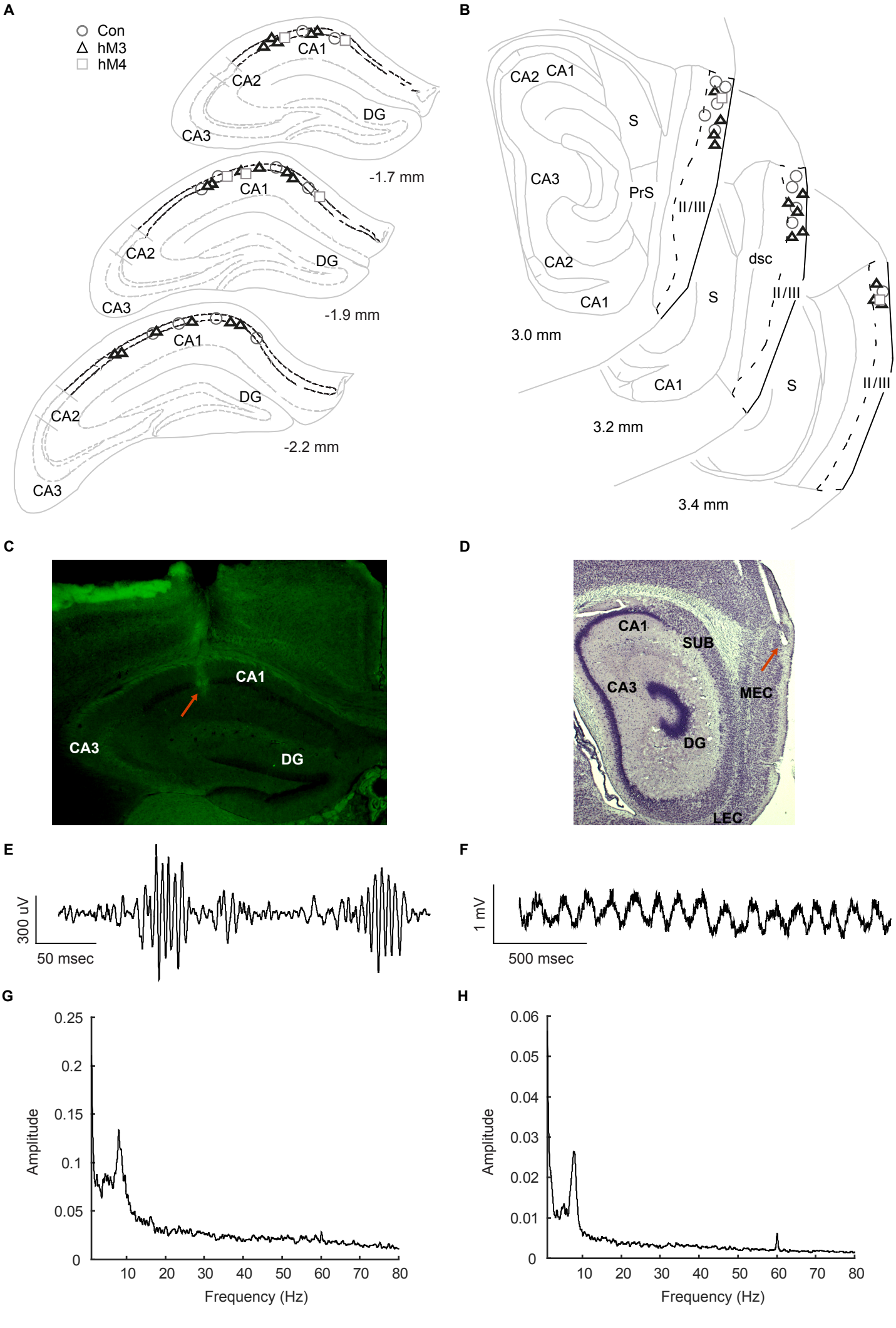
A
Con
hM3
hM4
CA1
CA2
DG
CA3
-1.7 mm
-1.9 mm
-2.2 mm
B
CA2
CA1
S
CA3
PrS
II/III
dsc
3.0 mm
3.2 mm
3.4 mm
C
CA1
CA3
DG
D
CA1
SUB
CA3
MEC
DG
LEC
E
300 uV
50 msec
F
1 mV
500 msec
G
Amplitude
Frequency (Hz)
H
Amplitude
Frequency (Hz)

Figure S2

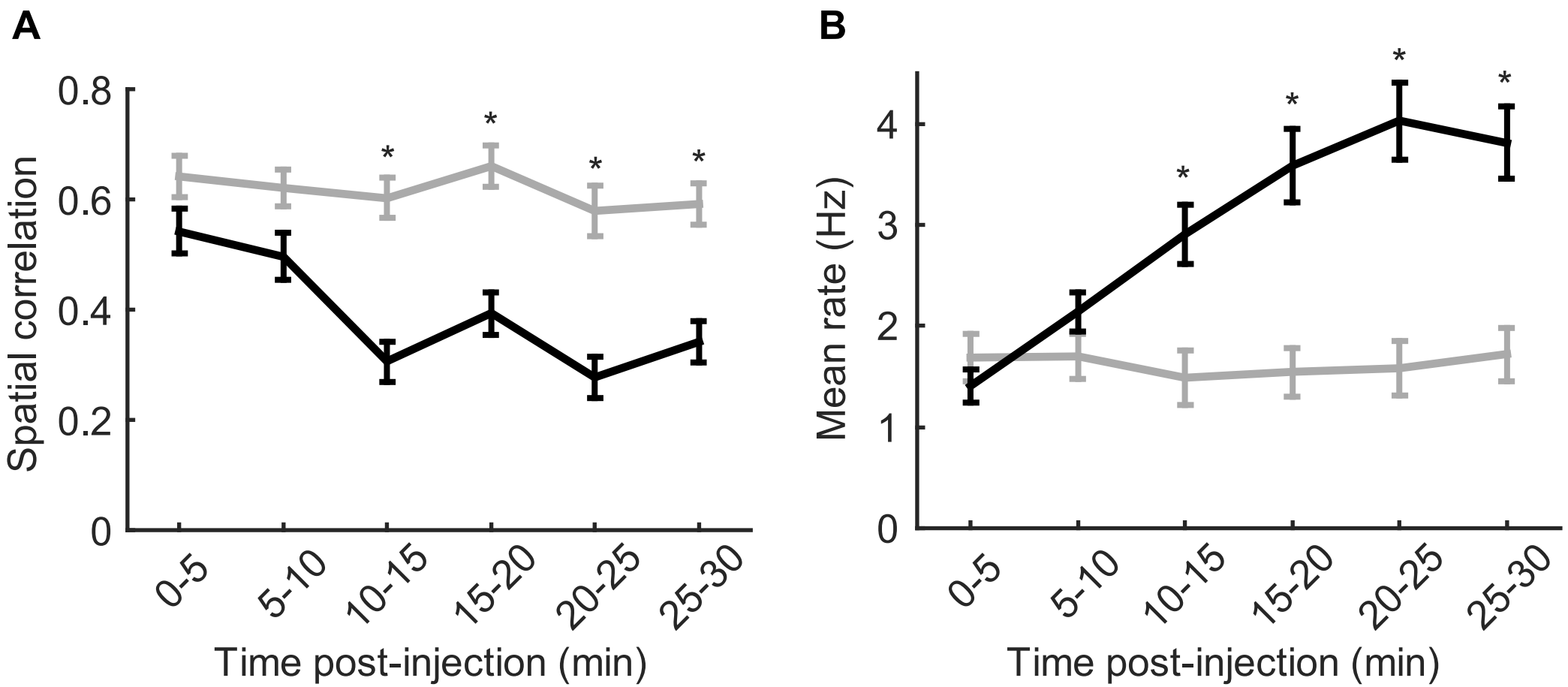
A
Spatial correlation
0.8
0.6
0.4
0.2
0
*
*
*
*
0-5
5-10
10-15
15-20
20-25
25-30
Time post-injection (min)
B
Mean rate (Hz)
4
3
2
1
0
*
*
*
*
0-5
5-10
10-15
15-20
20-25
25-30
Time post-injection (min)

Figure S3

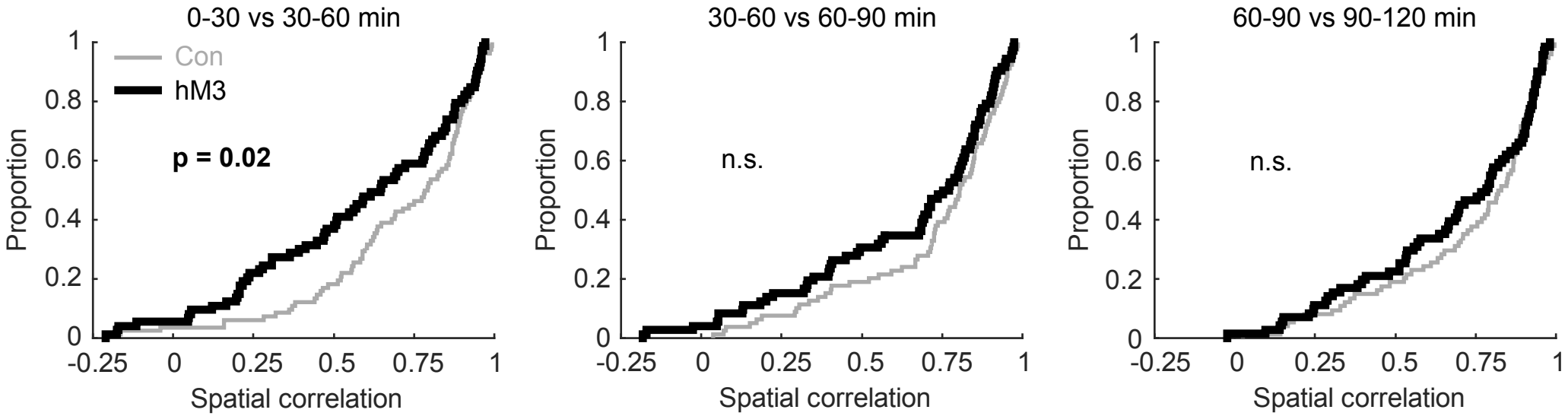
0-30 vs 30-60 min
Con
hM3
p = 0.02
Proportion
Spatial correlation
30-60 vs 60-90 min
n.s.
Proportion
Spatial correlation
60-90 vs 90-120 min
n.s.
Proportion
Spatial correlation

Figure S4

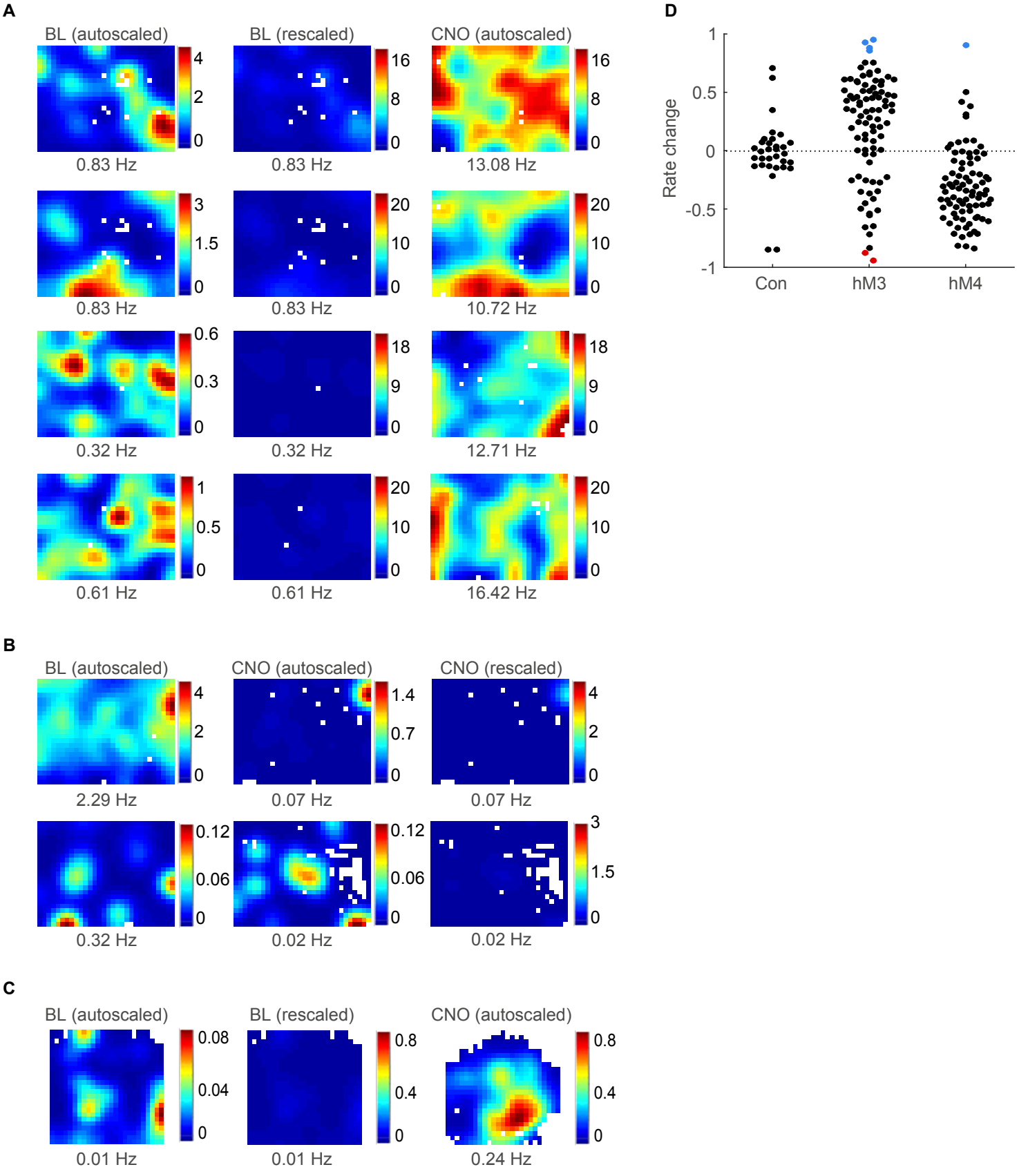
A
BL (autoscaled)
BL (rescaled)
CNO (autoscaled)
0.83 Hz
0.83 Hz
13.08 Hz
0.83 Hz
0.83 Hz
10.72 Hz
0.32 Hz
0.32 Hz
12.71 Hz
0.61 Hz
0.61 Hz
16.42 Hz
B
BL (autoscaled)
CNO (autoscaled)
CNO (rescaled)
2.29 Hz
0.07 Hz
0.07 Hz
0.32 Hz
0.02 Hz
0.02 Hz
C
BL (autoscaled)
BL (rescaled)
CNO (autoscaled)
0.01 Hz
0.01 Hz
0.24 Hz
D
Rate change
Con
hM3
hM4

Figure S5

SUPPLEMENTAL FIGURE LEGENDS

Figure S1, related to Figure 1. Visualization of hM3Dq transgene for cell counting.
Expression of hM3Dq transgene visualized by fluorescent RNA *in situ* and Nissl stain. D = dorsal, M = medial, MEC = medial entorhinal cortex, LEC = lateral entorhinal cortex, Sub = subiculum, Cb = cerebellum, ML = medial/lateral relative to midline.

Figure S2, related to Figures 2, 3, 5-8. Recording sites for electrophysiology experiments.
(A) Tetrode locations in CA1 identified in three coronal sections. Numbers indicate distance from bregma.
(B) Tetrode locations in MEC identified in three sagittal sections. S = subiculum, PrS = presubiculum, dsc = lamina dissecans. Numbers indicate distance from midline.
(C) Representative coronal section used to identify tetrode tracks in CA1.
(D) Representative sagittal section used to identify tetrode tracks in MEC.
(E) Example of awake hippocampal ripple recorded in CA1. Trace is local field potential after band-pass filtering in the ripple band (100 - 400 Hz).
(F) Example of strong theta rhythmicity recorded in MEC. Trace is broadband (0.1 - 475 Hz) local field potential.
Example power spectrum showing high amplitude in the theta band (6-10 Hz) in both CA1 (G) and MEC (H).
Red arrows in (C) and (D) indicate identified recording sites. DG = dentate gyrus, SUB = subiculum, MEC = medial entorhinal cortex, LEC = lateral entorhinal cortex.

Figure S3, related to Figures 2, 3, 5-8. Artificial remapping of place cells and increase in firing rate of excitatory MEC cells occur at the same time following CNO injection.
(A) Spatial correlation for CA1 place cells between baseline and 5-min epochs after CNO injection in Con (gray) and hM3 (black) mice.
(B) Mean firing rate of putative excitatory MEC neurons during 5-min epochs after CNO injection in Con (gray) and hM3 (black) mice.
Data represented as median ± SEM. *P < 0.05/n, one-sided Wilcoxon rank sum tests comparing hM3 to Con with Holm-Bonferroni correction for multiple comparisons.

Figure S4, related to Figures 2 and 3. Artificial remapping of place cells is stable 30 mins after CNO injection.
Cumulative distribution functions showing spatial correlation values between consecutive 30-min epochs following CNO injection in Con (gray) and hM3 (black) mice.
0-30 vs 30-60 min: D* = 0.2280, p = 0.0151; 30-60 vs 60-90 min: D* = 0.1670, p = 0.1142; 60-90 vs 90-120 min: D* = 0.1264, p = 0.2978; one-sided Kolmogorov-Smirnov tests.

Figure S5, related to Figures 6 and 8. A small proportion of MEC neurons exhibit large changes in mean firing rate following CNO injection.
Rate maps of cells which exceed the firing rate criterion of Kitamura et al. (2015).
(A) Four cells from hM3 mice significantly increased their firing rate following CNO injection, (B) two cells from hM3 mice significantly decreased their firing rate following CNO injection, and (C) one cell from an hM4 mouse significantly increased its firing rate following CNO injection.

(A-C) Each row is a cell and each column is the baseline or CNO session. Maps from sessions with lower firing rates are scaled both within session (autoscaled) and to the peak firing rate of the other session (rescaled) in order to visualize firing patterns. Red represents maximum firing, blue is silent, and white represents unvisited pixels. Mean rate indicated below rate maps.
(D) Change in mean firing rate for each MEC cell (putative excitatory and inhibitory) following CNO injection in Con, hM3, and hM4 mice. Cells which exceed the firing rate criterion are shown in blue (increases) and red (decreases). Note that the identified neurons do not appear to represent a unique population of MEC neurons, but rather they are likely the tails of a continuous distribution.

Table S1, related to Figures 2 and 3. Further characterization of CA1 neurons.
All statistical tests compare either hM3 or hM4 to Con mice. Statistically significant results ($\alpha = 0.05$) are in bold. Number of cells is indicated parenthetically following each group name. Mean values are reported for t-tests and median values are reported for rank sum tests. *Change* refers to a difference score (i.e. normalized change, see methods).

Measure	Mean/median ± SEM	Test	P value	Test statistic
Change in in-field firing rate (place cells)	Con (73) = -0.06 ± 0.03 hM3 (67) = 0.05 ± 0.04 hM4 (99) = -0.01 ± 0.03	Two-sided independent t-test	 p = **0.04** p = 0.27	 t(138) = 2.12 t(170) = 1.11
Change in spatial information (place cells)	Con (91) = -0.08 ± 0.02 hM3 (80) = -0.24 ± 0.03 hM4 (106) = -0.06 ± 0.02	Two-sided independent t-test	 p = **1.51×10^{-6}** p = 0.44	 t(169) = -4.99 t(195) = 0.78
Shift in location of peak rate (cm) (place cells) (bin width = 2 cm)	Con (91) = 11.66 ± 1.64 hM3 (80) = 23.11 ± 1.84 hM4 (106) = 8.89 ± 1.41	One-sided Wilcoxon rank sum test	 p = **2.89×10^{-4}** p = 0.72	 Z = 3.44 Z = -0.59
Change in number of firing fields (place cells)	Con (91) = 0 ± 0.03 hM3 (79) = 0 ± 0.03 hM4 (106) = 0 ± 0.03	Two-sided Wilcoxon rank sum test	 p = 0.10 p = 0.47	 Z = -1.67 Z = 0.73
Change in interneuron mean firing rate	Con (33) = -0.07 ± 0.03 hM3 (29) = -0.00 ± 0.03 hM4 (31) = -0.07 ± 0.03	Two-sided independent t-test	 p = 0.14 p = 1.00	 t(60) = 1.49 t(62) = 1.27×10^{-4}

Table S2, related to Figures 5-8. Further characterization of MEC neurons.
All statistical tests compare either hM3 or hM4 to Con mice. Statistically significant results ($\alpha = 0.05$) are in bold. Number of cells is indicated parenthetically following each group name. Number of spatial bins is indicated for population vectors. Mean values are reported for t-tests and median values are reported for rank sum tests. *Change* refers to a difference score (i.e. normalized, see methods) while *difference* refers to the raw difference. Grid cells were recorded from approximately three modules per group of mice.

Measure	Mean/median ± SEM	Test	P value	Test statistic
Population vector correlation (putative excitatory cells)	Con (1315) = 0.91 ± 0.00	One-sided Wilcoxon rank sum test		
	hM3 (690) = 0.60 ± 0.00		p = **1.13×10^{-281}**	Z = -35.84
	hM4 (1248) = 0.80 ± 0.00		p = **9.62×10^{-146}**	Z = -25.68
Difference in gridness	Con (9) = -0.09 ± 0.15	One-sided Wilcoxon rank sum test		
	hM3 (19) = -0.36 ± 0.16		p = 0.09	Z = -1.33
	hM4 (9) = -0.33 ± 0.25		p = 0.15	rank sum = 73
Difference in grid scale	Con (12) = 0.11 ± 1.01	Two-sided Wilcoxon rank sum test		
	hM3 (20) = -0.60 ± 0.86		p = 0.60	Z = -0.53
	hM4 (10) = -0.80 ± 2.12		p = 0.87	Z = -0.16
Grid rotation (degrees)	Con (12) = 1.16 ± 3.65	One-sided Wilcoxon rank sum test		
	hM3 (20) = 0.96 ± 2.99		p = 0.52	Z = -0.04
	hM4 (10) = 8.44 ± 4.35		p = **0.02**	Z = 2.15
Grid translation (cm) (bin width = 4 cm)	Con (13) = 1.70 ± 4.31	One-sided Wilcoxon rank sum test		
	hM3 (21) = 3.64 ± 3.32		p = **0.02**	Z = 2.13
	hM4 (11) = 1.79 ± 0.98		p = 0.57	Z = -0.17

Difference in border score	Con (3) = -0.02 ± 0.04 hM3 (14) = -0.02 ± 0.14 hM4 (27) = -0.05 ± 0.06	One-sided Wilcoxon rank sum test	 p = 0.48 p = 0.24	 rank sum = 125 Z = -0.69
Difference in preferred angle (degrees) (HD cells)	Con (24) = 3.34 ± 10.39 hM3 (55) = 3.36 ± 6.30 hM4 (54) = 2.24 ± 6.80	One-sided Wilcoxon rank sum test	 p = 0.31 p = 0.37	 Z = 0.49 Z = 0.33
Difference in mean vector length	Con (24) = 0.02 ± 0.05 hM3 (58) = -0.03 ± 0.02 hM4 (53) = -0.02 ± 0.03	One-sided Wilcoxon rank sum test	 p = 0.42 p = 0.37	 Z = -0.20 Z = -0.34
Difference in speed score	Con (50) = 0.01 ± 0.01 hM3 (94) = -0.01 ± 0.01 hM4 (84) = 0.03 ± 0.01	One-sided independent t-test	 p = 0.07 p = 0.92	 t(142) = -1.51 t(32) = 1.38
Change in grid cell mean firing rate	Con (9) = -0.06 ± 0.04 hM3 (21) = 0.00 ± 0.11 hM4 (11) = -0.39 ± 0.09	Two-sided Wilcoxon rank sum test	 p = 0.86 p = **0.02**	 Z = 0.18 Z = -2.36
Change in border cell mean firing rate	Con (3) = -0.19 ± 0.08 hM3 (14) = 0.41 ± 0.12 hM4 (30) = -0.46 ± 0.06	Two-sided Wilcoxon rank sum test	 p = 0.20 p = 0.25	 rank sum = 137 Z = -1.16
Change in HD cell mean firing rate	Con (10) = 0.01 ± 0.17 hM3 (58) = 0.32 ± 0.07 hM4 (54) = -0.38 ± 0.05	Two-sided Wilcoxon rank sum test	 p = 0.46 p = **0.03**	 Z = 0.74 Z = -2.15

Change in interneuron mean firing rate	Con (4) = 0.02 ± 0.04 hM3 (8) = 0.11 ± 0.04 hM4 (14) = -0.35 ± 0.07	Two-sided Wilcoxon rank sum test	 p = 0.11 p = **0.02**	 rank sum = 62 rank sum = 110